



## ORIGINAL ARTICLE

# Structural modifications and biomedical applications of $\pi$ -extended, $\pi$ -fused, and non-fused tetra-substituted imidazole derivatives



Sivaraman Somasundaram<sup>a,1</sup>, Sri Renukadevi Balusamy<sup>b,1,\*</sup>, Haribalan Perumalsamy<sup>c,d</sup>, Anuj Ranjan<sup>e</sup>, Qamar Abbas<sup>f</sup>, Navabshan Irfan<sup>g</sup>, Rajeshkumar Shanmugam<sup>h</sup>, Sanghyuk Park<sup>a,\*</sup>

<sup>a</sup> Department of Chemistry, Kongju National University, 56 Gongjudaehak-ro, Gongju, Chungnam 32588, Republic of Korea

<sup>b</sup> Department of Food Science and Biotechnology, Sejong University, Gwangjin-gu, Seoul 05006, Republic of Korea

<sup>c</sup> Center for Creative Convergence Education, Hanyang University, Seoul 04763, Republic of Korea

<sup>d</sup> Research Institute for Next Generation Material Design, Hanyang University, Seoul 04763, Republic of Korea

<sup>e</sup> Academy of Biology and Biotechnology, Southern Federal University, Stachki 194/1, Rostov-on-Don 344090, Russia

<sup>f</sup> Department of Biological Sciences, Kongju National University, 56 Gongjudaehak-ro, Gongju, Chungnam 32588, Republic of Korea

<sup>g</sup> Crescent School of Pharmacy, Crescent Institute of Science and Technology, Vandalur, Chennai-48, Tamilnadu, India

<sup>h</sup> Department of Pharmacology, Saveetha Dental College & Hospitals, Saveetha Institute of Medical and Technical Sciences (SIMATS), Chennai, Tamil Nadu, India

Received 9 January 2023; accepted 20 May 2023

Available online 30 May 2023

## KEYWORDS

Imidazole molecules;  
ESIPT;  
DFT/TD-DFT;  
Urease inhibition;  
Anti-cancer;  
Molecular docking

**Abstract** In this present study, we have designed, synthesized twenty three tetra-substituted-imidazole-based fluorescent dyes that belongs to three different families of  $\pi$ -extended,  $\pi$ -fused, and non-fused tetra-substituted derivatives, to investigate their photophysical and biological properties namely anti-cancer and urease inhibitory activity. The impact of structural variation on photophysical properties, and their association with solvent's polarity, and proticity were thoroughly examined by comparing with their analogues of blocked ESIPT functionality. Further, they were studied experimentally by means of absorption and fluorescence spectra monitoring through different solvent systems as well as theoretically by density functional theory/time dependent-density functional theory (DFT/TDDFT) calculations, respectively. For the evaluation of biological properties of imi-

\* Corresponding authors.

E-mail addresses: [renubalu@sejong.ac.kr](mailto:renubalu@sejong.ac.kr), [spark0920@kongju.ac.kr](mailto:spark0920@kongju.ac.kr) (S.R. Balusamy), [renubalu@sejong.ac.kr](mailto:renubalu@sejong.ac.kr), [spark0920@kongju.ac.kr](mailto:spark0920@kongju.ac.kr) (S. Park).

<sup>1</sup> These authors contributed equally to this manuscript.

Peer review under responsibility of King Saud University.



Production and hosting by Elsevier

dazole molecules, urease inhibitory activity of the imidazole derivatives against urease protein 4H9M was investigated through docking and *in vitro* studies. Among the synthesized compounds, AHPI-Br and POMPI-F showed the most effective urease inhibitory activity with  $IC_{50}$  values of  $0.0288 \pm 0.0034$  and  $0.0289 \pm 0.0025$   $\mu$ M and provided the highest docking scores. Moreover, anti-cancer activity of PHPI-I and PHPI-CI imidazole derivatives was confirmed by cytotoxic, and fluorescence analysis in stomach cancer cell lines (AGS). Our results demonstrated that PHPI-I, PHPI-CI exhibited significant apoptotic mediated cell death compared to all other imidazole groups in both *in vitro* and *in silico* analysis. Our present study concluded that synthesis of imidazole derivatives have ability to inhibit urease enzyme activity and anti-cancer activity *in vitro* and can act as a potential therapeutic targets and warrants *in vivo* studies.

© 2023 The Author(s). Published by Elsevier B.V. on behalf of King Saud University. This is an open access article under the CC BY-NC-ND license (<http://creativecommons.org/licenses/by-nc-nd/4.0/>).

## 1. Introduction

Substituted imidazole derivatives are one of the significant classes of heterocyclic scaffolds which plays an important core fragment of a wide range of natural products and biological system (Alghamdi et al., 2021; Daraji et al., 2019) (Luca, 2006; Zhu and Bienaymé, 2006) Such imidazole analogues are also biologically active compounds and possess a broad spectrum of biological activities such as anti-cancer, anti-inflammatory, analgesics, fungicidal, anti-bacterial, and plant growth regulations (Blevins et al., 2019; Dao et al., 2015; Zhao et al., 2018). After the investigation of facile synthetic methods which are pioneered by Debus (Wang et al., 2017) (and Radziszewski (Freedman and Loscalzo, 2016), the intriguing photophysical properties of 2,4,5-trisubstituted and 1,2,4,5-tetrasubstituted imidazoles have gained substantial attractions among researchers in recent decades (Dipake et al., 2022; Mirjalili et al., 2012). Recently, extensive ingenious researches are reported by several research groups to fabricate white light-emitting materials through a combination of proton transfer and restricted energy transfer using such kind of imidazole scaffolds with suitable donor–acceptor substituents (Huang et al., 2012; Mikhaylov et al., 2020; Tolomeu and Fraga, 2023).

The excited-state intramolecular proton transfer (ESIPT) has gained considerable attraction from theoretical as well as experimental perspectives due to its large Stoke's shifted fluorescence emission. Most of the ESIPT reactions involve proton transfer from a pre-existing hydrogen bond, giving rise to proton-transferred keto tautomer in the excited state, and therefore widely accepted as an interesting phenomenon (Hristova et al., 2015; Huang et al., 2012). Due to their drastic structural alternation, the keto (K) tautomer possesses different photophysical properties from that of the original (enol (E)) species, offering great versatility in a variety of applications such as lasing materials (Chen et al., 2014; Elsässer and Becker, 2013; Hsieh et al., 2010; Huang et al., 2017; Lin et al., 2010; Machado et al., 2021)), UV photostabilizers (Scarpin et al., 2021), optical filters (Kuila et al., 1999; Tsentalovich et al., 2006), radiation scintillators (Sherin et al., 2009, 2008), molecular recognition, and fluorescent probes respectively (Uenuma et al., 2021). The most recent cutting edge application have mainly focused on the lighting materials (Murata et al., 2007). The ultrafast rate of ESIPT, together with a large Stokes' shift between absorption and tautomer emission (peak-to-peak) provides a broad spectral window to fill in other complementary emissions from energy transfer and reabsorption. Many functional dyes display ESIPT, (e.g. flavones (Pariat et al., 2021)), 10-hydroxybenzo[h]quinoline (Kim et al., 2011), imidazo[1,2-a]pyridines (Park et al., 2009), 2-hydroxyphenylbenzoxazoles, and 2-(2-hydroxyphenyl) imidazole analogues are known to exhibit a high fluorescence quantum yields (Sun et al., 2009). Therefore, it will be more fascinating to understand the structure–property relationship of this category of compounds owing to its impact of  $\pi$  nature of the tetra-substituted imidazoles on the photophysical properties with solvent effect (Hariharan et al., 2018). Additionally, the substituted imidazole derivatives are one of

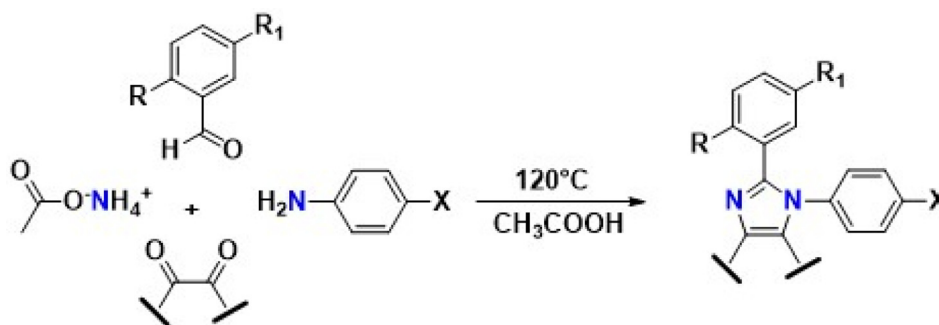
the most significant pharmacologically active compounds of natural products (Gurudutta et al., 2005; Kim et al., 2005, 2011; Park et al., 2009; Peng et al., 2011; Serdaliyeva D, Nurgozhin T, Satbayeva E, Khayitova M, Seitallyeva A, 2022; Sharma et al., 2016; Sun et al., 2009), and the members of this category are well-known to possess nitric oxide synthase inhibition, anti-mycotic, anti-biotic, anti-ulcerative, and CB1 receptor antagonistic activities (Serdaliyeva D, Nurgozhin T, Satbayeva E, Khayitova M, Seitallyeva A, 2022; Sharma et al., 2016; Wang et al., 2002), together with inhibitor activities of p38 MAP kinase (Magnus et al., 2006; Takle et al., 2006),  $\beta$ -Raf kinase (Naureen et al., 2015), glucagon receptors (de Laszlo et al., 1999), and therapeutic agents (Heeres et al., 1979). Similarly, substituted benzimidazole derivatives (Schmierer et al., 1988; Sharma et al., 2021) and the tetra-substituted imidazole derivatives (Heeres et al., 1979) (Ali et al., 2017) were reported to possess  $\alpha$ -glycosidase, anti-cancer and urease, respectively. Keeping all the above considerations, our research group have designed, synthesized, and characterized these  $\pi$ -extended phenanthro[9,10-d],  $\pi$ -fused acenaphtho[1,2-d], and non-fused tetra-substituted imidazole derivatives. Along with experimental studies, semi-empirical calculations were also carried out using density functional theory (DFT) and time-dependent density functional theory (TD-DFT), especially about critical hydrogen bonding by changing the ground and excited state geometry and Mulliken charge distribution analysis. Finally, the urease inhibitory activity and anti-cancer properties of ESIPT molecules were evaluated by *in vitro* and *in silico* method.

## 2. Results and discussion

### 2.1. Chemistry

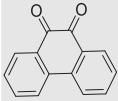
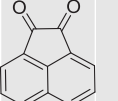
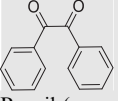
Scheme 1 illustrates the synthetic routes and the molecular structures of tetra-substituted imidazole derivatives, and the detailed molecular information are listed in Table 1. From the literature, the absorption and emission wavelength range of HPI and its derivatives are at 300–320 nm and 460–570 nm, respectively (Skonieczny et al., 2012). We have synthesized these imidazole derivatives based on the presence and nature of  $\pi$ -fusion, and  $\pi$ -extension of the chromophore would determine the photophysical properties, and therefore recommended the selection of different kinds of 1,2-diketones. To identify the substitution effect of 4-halophenyl group on the 1-position of imidazole and block of hydroxyl group, a library of twenty-three tetra-substituted imidazole molecules were synthesized with three different categories of 1,2-diketones such as  $\pi$ -non fused benzil,  $\pi$ -fused acenaphthoquinone, and  $\pi$ -extended 1,10-phenanthroquinone, as shown in Fig. 1.

The designed imidazole compounds were synthesized *via* classical Debus-Radziszewski one-pot multi-component reac-



**Scheme 1** Synthesis of  $\pi$ -extended phenanthro[9,10-d],  $\pi$ -fused acenaphtho[1,2-d], and  $\pi$ -non fused tetra-phenyl imidazoles.

**Table 1** Imidazole derivatives and their functional groups.

S. No.	Compound Name	$\alpha$ -diketone	R	R <sub>1</sub>	X
1	PTPI-F	 Phenanthroquinone ( $\pi$ -extended)	H	H	F
2	POMPI-F		OCH <sub>3</sub>	H	F
3	PHPI		OH	H	H
4	PHPI-F		OH	H	F
5	PHPI-Cl		OH	H	Cl
6	PHPI-Br		OH	H	Br
7	PHPI-I		OH	H	I
8	ATPI-F	 Acenaphthoquinone ( $\pi$ -fused)	H	H	F
9	AOMPI-F		OCH <sub>3</sub>	H	F
10	AHPI		OH	H	H
11	AHPI-F		OH	H	F
12	AHPI-Cl		OH	H	Cl
13	AHPI-Br		OH	H	Br
14	AHPI-I		OH	H	I
15	AHPI-EtoAc	OH	H	CH <sub>2</sub> CH <sub>2</sub> OCOCH <sub>3</sub>	
16	AMHPI	OH	OCH <sub>3</sub>	H	
17	BTPI-F	 Benzil ( $\pi$ -non fused)	H	H	F
18	BOMPI-F		OCH <sub>3</sub>	H	F
19	BHPI		OH	H	H
20	BHPI-F		OH	H	F
21	BHPI-Cl		OH	H	Cl
22	BHPI-Br		OH	H	Br
23	BHPI-I		OH	H	I

tion from 1,2-diketones with corresponding aromatic aldehydes, aromatic amines, and ammonium acetate with refluxing in acetic acid. The products were isolated with relatively good yield (65 to 75%) and single clean crystal was obtained from ethyl acetate by slow evaporation technique. The obtained imidazole derivatives were characterized by <sup>1</sup>H and <sup>13</sup>C NMR spectroscopy (Fig. S1–S46), GC–MS spectroscopy, and elemental analysis (EA). The <sup>1</sup>H and <sup>13</sup>C NMR spectra of all compounds are in agreement with the molecular structure, and chemical shifts of the resonance associated with the proton and carbon atoms of these molecules are in the acceptable range. The molecular mass of all the compounds corresponds to the mass spectrum results. Single crystal X-ray crystallography was used to confirm further the solid-state geometry of some of the representative imidazole molecules such as AHPI-F, AHPI-Cl, AHPI-Br, BHPI-Cl, and BHPI-Br and these results were already reported in our previous publications. (Parkin et al., 2001; Somasundaram et al., 2017). The

crystallographic results revealed that crystals of AHPI-F, AHPI-Cl, and AHPI-Br are in monoclinic crystal system with P2<sub>1/c</sub> space group and the crystals of BHPI-Cl and BHPI-Br are orthorhombic crystal system with P2<sub>1</sub>2<sub>1</sub>2<sub>1</sub> space group.

## 2.2. ESIPT phenomenon

All the synthesized imidazole molecules except ATPI-F, AOMPI-F, BTPI-F, BOMPI-F, PTPI-F and POMPI-F are possessing an acidic hydroxyl group at the *ortho*-position to phenyl ring which is directly attached to the imidazole core at position 2'. The existence of the intramolecular hydrogen bonding in the ground state is supported by the location of hydroxyl (–OH) and imine (=N–) groups as illustrated in the Fig. 2. During photoexcitation, the imine group (=N–), and the hydroxyl (–OH) group tend to become strong basic and acidic respectively as shown by the changes in the ground and excited states by Mulliken charge distribution (Table 2).

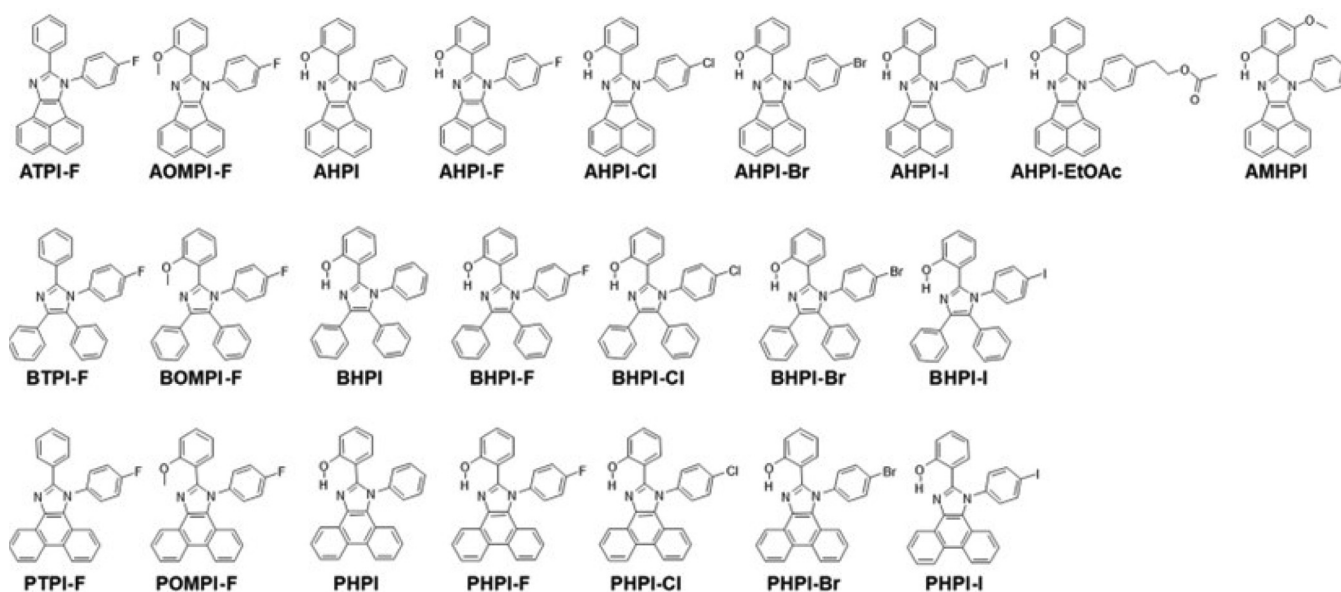


Fig. 1 Molecular structures of  $\pi$ -Extended,  $\pi$ -fused, and non-fused tetra-substituted imidazole derivatives.

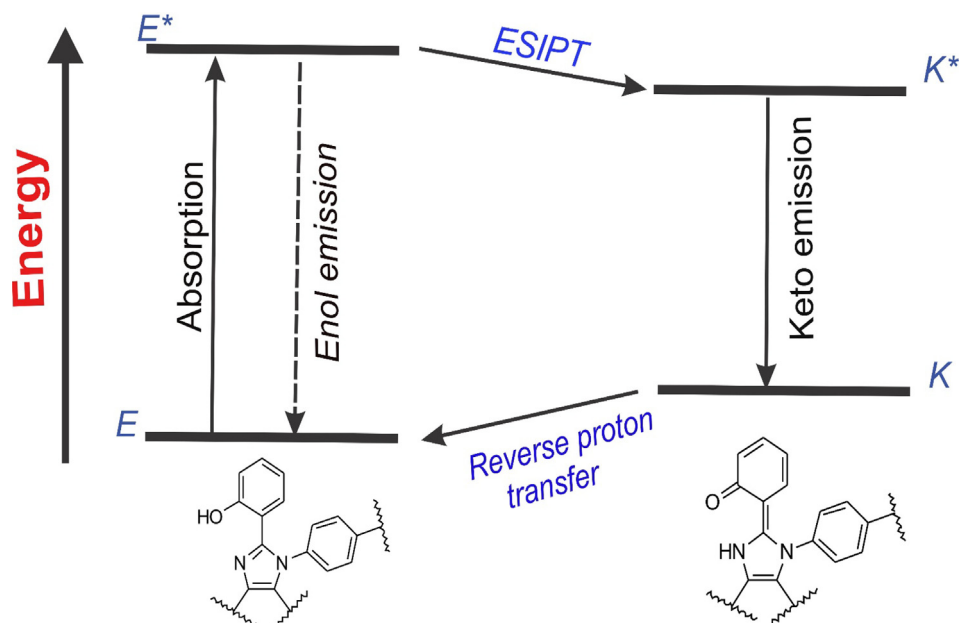


Fig. 2 Pictorial expression of 4-level ES IPT process and the intramolecular hydrogen bonding in the tetra-substituted imidazole system.

Due to this, the excited-state enol form ( $E^*$ ) is converted to the excited-state keto form ( $K^*$ ) (Fig. 1) which results in the ES IPT. Briefly, upon UV light irradiation, absorption of light excites the ground state enol ( $E$ ) state to the excited state ( $E^*$ ). Then, the  $E^*$  either undergoes mainly the ES IPT by fast proton transfer to  $K^*$  or returns to the ground state enol ( $E$ ) form by emitting the 'enol' emission ( $E^* \rightarrow E$ ). After ES IPT process, the excited keto form ( $K^*$ ) returns to the keto ground state ( $K$ ) by releasing its radiation, which is called the 'keto' emission ( $K^* \rightarrow K$ ). By this way of the 4-level ES IPT process (Fig. 2), these molecules exhibit absorption and characteristic large stokes shifted emission.

### 2.3. Photophysical properties

The absorption and emission spectra of all the imidazole derivatives were studied in a dilute solution ( $10^{-5} \text{ mol L}^{-1}$ ) of three categories of solvents with different proticity and dielectric constants, non-polar chloroform ( $\text{CHCl}_3$ ), polar protic ethanol (EtOH) and polar aprotic acetonitrile (MeCN) at room temperature. To understand the complexity of the ES IPT process of synthesized imidazole derivatives and its efficiency under internal and external parameters such as structural modification and solvent nature, we compared the spectral properties with non-ES IPT analogues. Molar absorp-

**Table 2** The calculated Mulliken charges (in a.u) of the hydroxyl moiety O atom and neighbouring N atom for  $\pi$ -fused acenaphtho [1,2-d]imidazole,  $\pi$ -extended phenanthro[9,10-d] and  $\pi$ -non fused tetra substituted imidazole in S0 and S1 state at B3LYP/6-31G (d,p) level.

S. No.	Compounds	Oxygen		Nitrogen	
		S <sub>0</sub>	S <sub>1</sub>	S <sub>0</sub>	S <sub>1</sub>
1	ATPI-F	–	–	–	–
2	AOMPI-F	–	–	–	–
3	AHPI	–0.770	–1.268	–0.592	–1.730
4	AHPI-F	–0.790	–0.771	–0.595	–0.982
5	AHPI-Cl	–1.110	–0.771	–0.594	–1.408
6	AHPI-Br	–0.780	–0.771	–0.594	–0.981
7	AHPI-I	–0.630	–0.625	–0.595	–0.717
8	AHPI-EtoAc	–0.780	–0.771	–0.593	–0.980
9	AMHPI	–0.80	–0.786	–0.591	–0.978
10	BTPI-F	–	–	–	–
11	BOMPI-F	–	–	–	–
12	BHPI	–0.780	–0.637	–0.747	–0.973
13	BHPI-F	–0.77	–0.783	–0.73	–0.973
14	BHPI-Cl	0.636	–0.783	0.746	–0.975
15	BHPI-Br	–0.77	–0.783	–0.729	–0.976
16	BHPI-I	–0.64	–0.783	–0.746	–0.975
17	PTPI-F	–	–	–	–
18	POMPI-F	–	–	–	–
19	PHPI	–0.77	–0.765	–0.699	–0.858
20	PHPI-F	0.771	–0.765	0.702	–0.861
21	PHPI-Cl	–0.77	–0.765	–0.702	–0.861
22	PHPI-Br	–0.77	–0.765	–0.701	–0.860
23	PHPI-I	–0.77	–0.765	–0.702	–0.861

tivity and corresponding absorption maxima, emission maxima, Stokes' shifts, and fluorescence quantum yields are given in Table S1-S3.

The absorption and emission spectra of  $\pi$ -extended phenanthro[9,10-d],  $\pi$ -fused acenaphtho[1,2-d], and  $\pi$ -non fused tetra substituted imidazole series were studied in Fig. S47–S49. The respective absorption spectra are characterized by a band in the 250–400 nm range which are due to a  $\pi \rightarrow \pi^*$  transition corresponding to excitation of aromatic electrons (Fig. 2). The absorption band around 300 nm (ATPI-F, AOMPI-F), 250 nm (BTPI-F, BOMPI-F), and 320 nm (PTPI-F, POMPI-F) are probably due to neutral/unsolved open conformer of non-ESIPT system. The absorption maxima are negligibly sensitive to solvent polarity (Alarcos et al., 2015; Chowdhury et al., 2003; Mahanta et al., 2006; Singh et al., 2007; Wu et al., 2004). The slight redshifts of AHPI, BHPI and PHPI series compared to the ATPI-F, AOMPI-F, BTPI-F, BOMPI-F, PTPI-F and POMPI-F due to the presence of an intramolecular hydrogen bond making larger the  $\pi$  electronic configuration. On other hand, the insensitivity of the absorption spectra of these molecules to the solvent polarity indicates that the dipole moments of compounds in the ground state are nearly identical. The presence of halogen and ester functional groups in all AHPI-F, AHPI-Cl, AHPI-Br, AHPI-EtoAc, BHPI-F, BHPI-Cl, BHPI-Br, BHPI-I, PHPI-F, PHPI-Cl, PHPI-Br, and PHPI-I exhibits the S<sub>0</sub>  $\rightarrow$  S<sub>1</sub> transition, which is relatively the same energies with their parent molecules as AHPI, BHPI and PHPI (whose absorption maximum is around 325 nm, 320 nm and 365 nm) (Skonieczny

et al., 2012). In AMHPI absorption spectrum, hypsochromic shift was observed in chloroform, while ATPI-F showed bathochromic shifted absorption in ethanol solvent system. This variation is ascribable to the intermolecular interaction between solvent system and fluorescent molecules.

The fluorescence emission spectra of all  $\pi$ -extended phenanthro[9,10-d],  $\pi$ -fused acenaphtho[1,2-d], and  $\pi$ -non fused tetra-phenyl substituted imidazole molecules consists of a unique band whose maximum is also shifted with the solvent effect. A prominent single emission peak in the range of 450–600 nm was observed in all the samples. The presence of these unique Stokes' shifted emission peaks indicated that the fluorescence property of these molecules was not quenched (except AOMPI-F (in CHCl<sub>3</sub>), AMHPI (in CHCl<sub>3</sub>, MeCN, and EtOH) even in solid-state. In nonpolar organic solvents, all the compounds of AHPI, BHPI, and PHPI series showed the emission at 569 nm, 469–483 nm, and 477 nm, respectively.

Similarly, in polar protic solvent and a polar aprotic solvent such as EtOH and MeCN, emission band at around 578 nm (AHPI series), 474 nm (BHPI series), 477–480 nm (PHPI series), and 556–560 nm (AHPI series), 474 nm (BHPI series) (PHPI series) were observed (Fig. S47–S49). The keto emission shows a remarkable redshift from 556 nm (in EtOH) to 572 nm (in CHCl<sub>3</sub>) due to intermolecular interaction between solvent molecules and imidazoles, and similar emission properties are reported by Skonieczny et al. (Skonieczny et al., 2012). The emission of all compounds at > 450 nm can be assigned to the radiative decay of the excited keto tautomer (K\*). The emission of ATPI-F, AOMPI-F, BTPI-F, BOMPI-F, PTPI-

F, and POMPI-F confirmed these postulations. Compounds with a protected hydroxyl group (AOMPI-F, BOMPI-F, and POMPI-F) and without hydroxyl group (ATPI-F, BTPI-F, and PTPI-F) showed almost same emission in both protic and aprotic solvents, indicating the absence of ESIPT. From the photoluminescence (PL) spectroscopy results, the emission shift tendency can be concluded to following order of  $\pi$ -fused acenaphtho[1,2-d]imidazoles >  $\pi$ -extended phenanthro[9,10-d]imidazoles >  $\pi$ -non fused tetra phenyl substituted imidazoles. The longer emission of  $\pi$ -fused and  $\pi$ -extended system of imidazoles is probably due to the high  $\pi$ - $\pi$  stacking interaction of planar geometry. The  $\pi$ -non fused system has relatively shorter emission wavelength compared to the other two systems. On the other hand, the large Stokes shifted emission spectra (Table S1–S3) according to the increased number of conjugated aromatic ring systems reflected the existence of intramolecular charge transfer (ICT) which takes place in the excited state keto-enol tautomer, thus resulting in significant changes in the optical properties.

Fluorescence quantum yields ( $\phi_{\text{PL}}$ ) of compounds possessing  $\pi$ -fused acenaphtho[1,2-d]imidazole,  $\pi$ -extended phenanthro[9,10-d]imidazole and  $\pi$ -non fused tetra-phenyl substituted imidazole cores showed different characteristics due to its sensitivity to the solvent polarity (Table S1–S3). It is observed that the quantum yields are higher in polar aprotic solvents and this can be attributed to longer emission lifetime due to the hydrogen bond between molecule and solvent system. Comparably, quantum yields are the highest in acenaphtho[1,2-d]imidazole derivatives and the least in tetra-phenyl substituted imidazole derivatives.

#### 2.4. Electronic spectra and frontier molecular orbitals: Computational studies

Density functional theory (DFT) calculations were performed to characterize the optimized molecular geometries, frontier molecular orbital energy levels, and relative absorption spectra for  $\pi$ -extended phenanthro[9,10-d]imidazole,  $\pi$ -fused acenaphtho[1,2-d]imidazole, and  $\pi$ -non fused tetra phenyl substituted imidazoles at B3LYP/6–31 G (d, p) level by using Gaussian 09 program. The ground and excited state geometries of the fluorophores in both E and K forms were optimized with DFT/TD-DFT method. The theoretical UV–vis. absorption of synthesized compounds was calculated by TD-DFT method.

The DFT and TD-DFT method have been adopted to optimize the structure for the molecules in  $S_0$  and  $S_1$  state, respectively. The optimized geometries with intramolecular hydrogen bonds of AHPI, BHPI, and PHPI are shown in Fig. 3. Among twenty-three structures of stable isomers, we have displayed representative three molecules, because all the molecules of those three categories have similar geometry. To make the description of bond length and bond angle clearer and more concise, the hydrogen-bonded atoms have been numbered. We listed the most important structural parameters in Table 3, which were calculated by the B3LYP/6–31 G (d, p) basic set. Based on the calculated results, it is worth noting that the bond lengths of O1–H2, H2–N3 of phenanthro[9,10-d]imidazole are 0.964 Å, acenaphtho[1,2-d]imidazole structure is 0.968 Å, and tetraphenyl substituted imidazole is 0.972 Å in the ground state ( $S_0$ ) state, respectively. However, after being excited to

$S_1$  state, the bond lengths are 0.984 Å, 0.984 Å, and 0.981, respectively. Meanwhile, the O1–H2–N3 bond angle varies from 146.3 to 148.2°, 146.9–147.9° and 143.5–144° in  $S_1$  state to 122.6–122.7°, 123.1° and 132.3° in  $S_0$  state. Significantly, the bond length of O1–H2 is longer as well as H2–N3 is shorter in the excited  $S_1$  state, which indicates that the intramolecular hydrogen bonds are simultaneously enhanced in the excited  $S_1$  state and in the bond angle of O1–H2...N3 was higher than in  $S_0$  state respectively. From the above results, it is indicated that the intramolecular hydrogen bond O1–H2...N3 is more stable in the  $S_1$  state than that in the ground state.

The calculated absorption maxima (by TD-DFT-B3LYP/6-31G (d, p) theoretical level) of  $\pi$ -fused acenaphtho[1,2-d]imidazole,  $\pi$ -extended phenanthro[9,10-d]imidazole, and  $\pi$ -non fused tetra phenyl substituted imidazole is at 300–480 nm, 300–370 nm, and 324–569 nm, which is in good agreement with the experimental results. The prominent intense absorption can be assigned to HOMO–2 to LUMO transition and the other absorption arises from HOMO–LUMO transition. To further investigate the nature of the charge distribution and charge transfer in the electronically excited state, the frontier molecular orbital of all three imidazole families are depicted in Fig. 4. The calculated electronic excitation energies and corresponding oscillator strengths of the first three states for all molecules are listed in Table S1, S2, and S3. The oscillator strength of  $S_0 \rightarrow S_1$  transition of  $\pi$ -fused acenaphtho[1,2-d]imidazole,  $\pi$ -extended phenanthro[9,10-d] and  $\pi$ -non fused tetra substituted imidazole are 0.0644–0.0721, 0.2193–0.3099 and 0.0781–0.0922 respectively, showing that the enol-keto tautomer has a positive effect. According to Kasha's rules, we have discussed only the first electronic excited state (HOMO and LUMO energy levels) of the molecules. It is noted that, the HOMO orbitals of the studied molecular system are  $\pi$  type orbitals while the LUMO orbitals are  $\pi^*$  character, indicating that the first excited states are the  $\pi \rightarrow \pi^*$  type transition from HOMO to LUMO. The HOMO and LUMO are localized on different parts of the molecules. In addition, the H...N bonds in the LUMO orbital have  $\sigma$  character, showing that the N atoms with electron pair donation ability can form a covalent bond with the H atoms after photoexcitation to the  $S_1$  state. The electron density on the hydroxyl group decreases upon excitation, whereas the electron density on the N atom of imidazole moiety increased upon photoexcitation. The changes in the electron density indicated both the acidity of the hydroxyl group and the basicity of the N atom group have increased upon excitation, which coincides with the occurrence of ESIPT. The calculated Mulliken charges of the hydroxyl moiety O atom and the neighbouring N atom for all molecules except ATPI-F, AOMPI-F, BTPI-F, BOMPI-F, PTPI-F, and POMPI-F are shown in Table 2. Upon transition from the HOMO to LUMO, the decrease of electron density in the hydroxyl moiety and the increase in N atoms were expected to directly influence the intramolecular hydrogen bonding. That is, the H...N bonds length becomes shorter upon excitation to  $S_1$  state. From the viewpoint of the valence bond theory, the transition from  $S_0 \rightarrow S_1$  state leads to more negative charge contributed on the N atoms and the enlarged interaction between the lone pair electron of N atoms and the  $\sigma^*(\text{O–H})$  orbitals will facilitate ESIPT processes from O atom to N atom. Therefore, the ESIPT is expected to occur due to the intramolecular charge transfer.

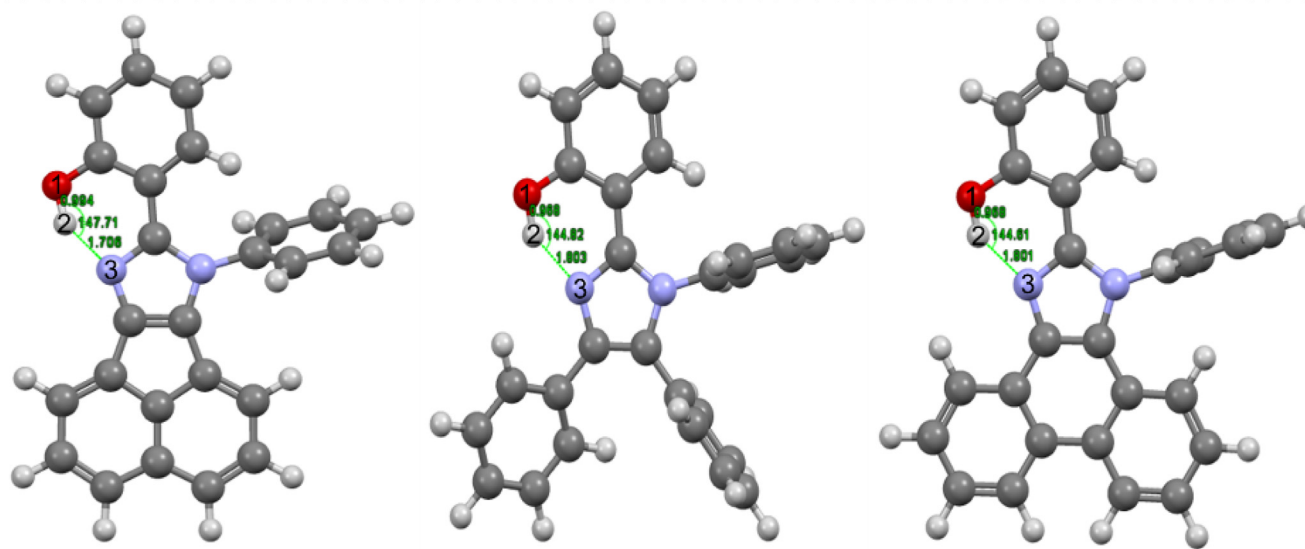


**Fig. 3** Optimized geometries of (a)  $\pi$ -extended phenanthro[9,10-d], (b)  $\pi$ -fused acenaphtho[1,2-d]imidazole, and (c)  $\pi$ -non fused tetra phenyl substituted imidazole using DFT calculations with the B3LYP/6-31 G(d,p) parameter. Red: O; white: H; Blue: N; gray: C atom.

**Table 3** The calculated bond length ( $\text{\AA}$ ) and bond angle ( $^\circ$ ) of  $\pi$ -fused acenaphtho[1,2-d]imidazole,  $\pi$ -extended phenanthro[9,10-d] and  $\pi$ -non fused tetra substituted imidazole in the  $S_0$  and  $S_1$  states.

S. No.	Compounds	O1-H2		H2-N3		$\delta$ (O1-H2-N3)	
		$S_0$	$S_1$	$S_0$	$S_1$	$S_0$	$S_1$
1	ATPI-F	–	–	–	–	–	–
2	AOMPI-F	–	–	–	–	–	–
3	AHPI	0.968	0.984	1.872	1.806	122.7	146.9
4	AHPI-F	0.968	0.984	1.873	1.810	122.7	146.8
5	AHPI-Cl	0.968	0.984	1.873	1.804	122.7	146.9
6	AHPI-Br	0.968	0.984	1.873	1.744	122.6	147.2
7	AHPI-I	0.968	0.984	1.873	1.795	122.7	148.2
8	AHPI-EtOAc	0.968	0.983	1.873	1.855	122.6	146.3
9	AMHPI	0.968	0.984	1.875	1.798	122.7	147.0
10	BTPI-F	–	–	–	–	–	–
11	BOMPI-F	–	–	–	–	–	–
12	BHPI	0.968	0.984	1.869	1.741	123.1	147.3
13	BHPI-F	0.968	0.984	1.870	1.741	123.1	147.3
14	BHPI-Cl	0.968	0.984	1.870	1.795	123.1	146.9
15	BHPI-Br	0.968	0.984	1.870	1.744	123.1	147.2
16	BHPI-I	0.968	0.984	1.870	1.743	123.1	147.3
17	PTPI-F	–	–	–	–	–	–
18	POMPI-F	–	–	–	–	–	–
19	PHPI	0.972	0.982	2.100	1.981	132.3	144.0
20	PHPI-F	0.972	0.981	2.195	2.002	132.3	143.5
21	PHPI-Cl	0.972	0.981	2.195	2.003	132.3	143.5
22	PHPI-Br	0.972	0.981	2.195	1.997	132.3	143.6
23	PHPI-I	0.972	0.981	2.195	2.001	132.3	143.5

### 2.5. Urease inhibition activity-Structural activity relationship (SAR)

The evaluation of urease inhibition was carried out for the synthesized twenty-three imidazole molecules of three different  $\pi$ -systems using thiourea as a reference standard which showed  $IC_{50}$  value of  $16.14 \pm 0.072 \mu\text{M}$  for this urease inhibition

experiments. These imidazole derivatives showed varying degrees of inhibition against urease activity in the range of  $0.0288 \pm 0.0034$  to  $0.1709 \pm 0.00496 \mu\text{M}$  respectively. Though the observed inhibition potential is the resultant of a whole molecule, a limited structure-activity relationship (SAR) was rationalized by considering the effect of different functional groups including hydroxyl, methoxy, halogens, acetoethyl

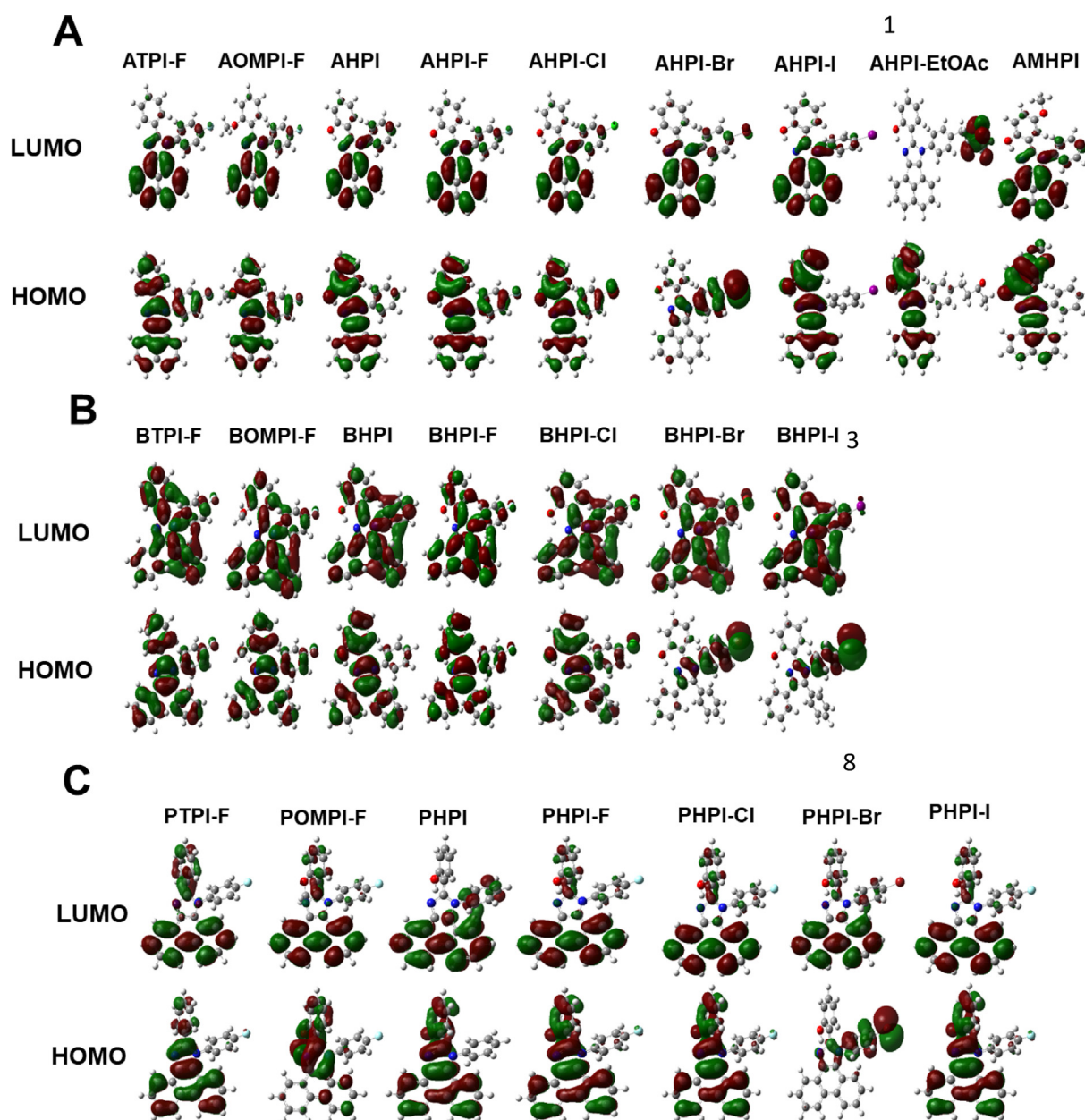


**Fig. 4** Calculated frontier molecular orbital diagram (Iso value 0.02) for **A.** acenaphthol [1,2-d]imidazole, **B.** Phenanthro [9,10-d]imidazole, and **C.** tetra phenyl substituted imidazole using TD-DFT/B3LYP (6-31 G) (d,p) theoretical level.

and the  $\pi$  nature such as extended, fused, and non-fused present in the imidazole on the inhibitory potential.

Amongst  $\pi$ -fused acenaphtho[1,2-d]imidazole compounds containing halogen atom (F, Cl, Br and I) in their respective imidazole N-substitution, inhibition potential varies due to presence of halogen atom and presence or absence of the *o*-hydroxy group in the phenyl ring substituted in 2-position to imidazole core. All imidazole molecules exhibited significant inhibitory activity compared to the standard thiourea except the compound ATPI-F, showed least inhibitory activity ( $IC_{50}$   $0.0474 \pm 0.00154 \mu\text{M}$ ) due to high electronegative fluorine atom and no OH group. Likewise, AMHPI and AHPI-EtOAc also showed decreased inhibition activity against urease due to the presence of  $-\text{OCH}_3$  donor group in para position to the  $-\text{OH}$  of AMHPI and  $-\text{EtOAc}$  group in N-

substitution of AHPI-EtOAc respectively. Whereas, POMPI-F ( $IC_{50}$   $0.0289 \pm 0.0025 \mu\text{M}$ ) and BTPI-F ( $IC_{50}$   $0.031 \pm 0.0127 \mu\text{M}$ ) exhibited the most significant inhibitory activity against urease among the other respective family of imidazole derivatives. The possible reason might be due to the interaction of OH and halogen groups on the aromatic system ( $\pi$ -fused acenaphtho and  $\pi$ -extended phenanthro system) that allowed to bind with nickel atom present in the urease enzyme. The urease activity of all the compounds shown in Table 4 compared with reference compound thiourea.

## 2.6. Kinetic mechanism

Based on the inhibitory potential, presently two compounds AHPI-Br and POMPI-F were studied for their mode of inhibi-



**Table 4** The inhibitory effect of Imidazole compounds on Urease (Jack bean) inhibition activity.

Compounds	Urease activity IC <sub>50</sub> ± SEM (μM)	Compounds	Urease activity IC <sub>50</sub> ± SEM (μM)	Compound	Urease activity IC <sub>50</sub> ± SEM (μM)
ATPI-F	0.0474 ± 0.00154	BTPI-F	0.031 ± 0.00127	PTPI-F	0.0522 ± 0.00154
AOMPI-F	0.039 ± 0.00125	BOMPI-F	0.041 ± 0.00142	POMPI-F	0.0289 ± 0.0025
AHPI	0.029 ± 0.0020	BHPI	0.0323 ± 0.0011	PHPI	0.0299 ± 0.0014
AHPI-F	0.089 ± 0.0047	BHPI-F	0.0318 ± 0.0021	PHPI-F	0.031 ± 0.0021
AHPI-Cl	0.0307 ± 0.0010	BHPI-Cl	0.1709 ± 0.00496	PHPI-Cl	0.0358 ± 0.00154
AHPI-Br	0.0288 ± 0.0034	BHPI-Br	0.0301 ± 0.0092	PHPI-Br	0.0451 ± 0.00156
AHPI-I	0.0473 ± 0.00021	BHPI-I	0.0701 ± 0.00094	PHPI-I	0.0681 ± 0.00165
AHPI-EtOAc	0.0506 ± 0.00176			Thiourea	16.14 ± 0.072
AMHPI	0.0807 ± 0.0028				

tion against urease. The potential of these two compounds to inhibit the free enzyme and enzyme-substrate complex was determined in terms of EI and ESI constants respectively. The kinetic studies of the enzyme by the Lineweaver-Burk plot of  $1/V$  versus  $1/[S]$  in the presence of different inhibitors concentrations gave a series of straight lines as shown in [Figure S50](#) (A) and (D) displayed compounds AHPI-Br and POMPI-F intersection within the second.

quadrant. The analysis showed that  $V_{max}$  decreased with increasing  $K_m$  in the presence of increasing concentrations of compounds AHPI-Br and POMPI-F. This behaviour of AHPI-Br and POMPI-F derivatives indicated that it inhibits the urease by two different pathways competitively forming enzyme inhibitor (EI) complex and causing the interruption of enzyme-substrate-inhibitor (ESI) complex in a non-competitive manner. The secondary plots of slope versus concentration of compounds such as AHPI-Br and POMPI-F showed EI dissociation constants  $K_i$  [Figure S50](#) (B) and (E) while ESI dissociation constants  $K_i'$  were shown by secondary plots of intercept versus concentration of compounds AHPI-Br and POMPI-F [Figure S50](#) (C) and (F). A lower value of  $K_i$  than  $K_i'$  pointed out stronger binding between enzyme and compounds API-Br and POMPI-F which suggested the competitive over non-competitive manners. The results of kinetic constants and inhibition constants are presented in [Table S4](#).

### 2.7. Docking studies

The docked files (ligand and receptor complex) were stored in .pdb format and visualized using a tool Discovery studio visualizer. The best poses were identified based on the number of interactions, a ligand has made and RMSD ([Table 5](#)). The identified pose was extracted for detailed observation and extracting the snaps. For the 3-D representation of binding of ligand was captured in 'solid ribbons presentation' of receptor and ligands were presented in "solid sticks presentation". The 2D interaction map was also captured.

**Bcl-xl:** Docking of Bcl-xl with PHPI-Cl observed a binding energy of  $-8.4$  kcal/mol as compared to PHPI  $-7.9$  kcal/mol. PHPI formed  $\pi$ -alkyl bonds with leu54 and Ala88; whereas Bcl-xl-PHPI-Cl formed Vander Waal bonds (Lys20),  $\pi$ -sigma (Ala50),  $\pi$ -aklyl (Ala95) ([Fig. 5](#)).

**Bcl-2:** Ligands PHPI-I and PHPI-Cl bound with Bcl-2 with a binding energy of  $-9.4$  kcal/mol however, PHPI exhibited binding energy of  $-8.9$  kcal/mol. PHPI interacted with Bcl-

2- with Glu209 by a  $\pi$ -anion, with Phe198 by  $\pi$ - $\pi$  and with Leu201 by  $\pi$ -alkyl interaction. No H-bonds were noticed. The ligand PHPI-Cl forms a conventional H-bond with Trp144 and a  $\pi$ -alkyl with Ala100 ([Fig. 6](#)).

**Urease:** The ligand AHPI-Br and POMPI-F bound to the defined active site by the binding energy  $-10.3$  kcal/mol as however, POMPI-F with urease exhibited  $-9.7$  kcal/mol with LB-RMSD 1.53 and 2.16 Å respectively. Urease with AHPI-Br formed mainly  $\pi$ -sigma (Val36, Ala37, Leu827, Met734, Lys704); whereas POMPI-F with urease formed  $\pi$ -cation (Lys704),  $\pi$ -alkyl (Ala37) and  $\pi$ -sigma (Leu827) ([Fig. 7](#)). Since, metal Ni is an important for urease for activity, hence observing interaction with Ni could be interesting. But, the presence of water molecules within the binding cavity is important for establishing the coordination of metal Ni ([Nim and Wong, 2019](#)). The lack of observed interaction with Ni in the docking process may be attributed to the non-aqueous environment used. However, molecular dynamic simulation of the docked complex for at least 200 ns could certainly provide further insights particularly regarding sustained interactions over the course of the simulation. Further, the interaction of OH and halogen groups can affect the inhibitory activity of urease ([Rashid et al., 2020](#); [Liu et al., 2020](#); [Chaudhry et al., 2020](#)). However, no such interaction has been observed in both POMPI-F and AHPI-Br ([Fig. 7](#)).

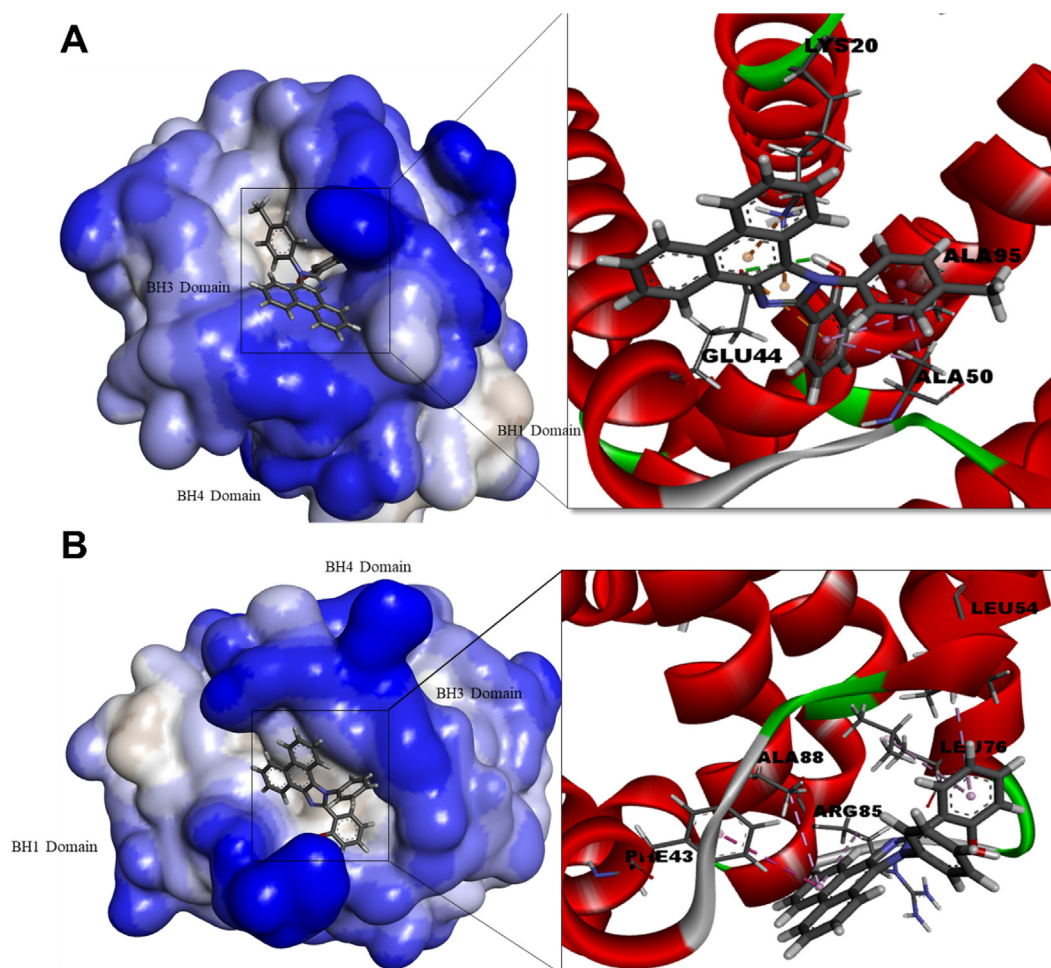
### 2.8. Anti-cancer activity

The MTT results showed the PHPI-I and PHPI-Cl possessed the strong anti-proliferative activity among other imidazole derivatives against AGS cell line in a dose-depending manner ([Fig. 8 A-C](#)). Later, the morphological observation of both untreated and treated AGS cell line was observed it showed significant induction of cell death compared with untreated cell lines ([Fig. 8C](#)). Cancer cells modulate the apoptosis process by regulating.

transcription, translation, and by post-translational modification and therefore causing cancer cells to escape apoptotic process ([Fernald and Kurokawa, 2013](#)). Determination of apoptotic cell death of detection on AGS cell line was performed by both hoechst and propidium iodide staining analysis. With or without PHPI-I or PHPI-Cl treatment (25 and 50  $\mu\text{g/ml}$ ), showed dose dependent visible chromatin condensation and degradation of nuclei in AGS cells ([Fig. 9](#)). When looking inside the cell, one of the most obvious features of

**Table 5** Docking result showing binding energy, RMSD, and the respective interacting residues.

Protein	Ligand	Binding energy (kcal/mol)	RMSD (LB)	RMSD (UB)	Interacting residues
BCI2	PHPI	-8.9	1.743	2.197	Phe198, Leu201, Glu209
BCI2	PHPI-Cl	-9.4	2.054	4.896	Ala100, Trp144, Phe198, Leu201, Glu209
BCI-XI	PHPI	-7.9	2.257	5.24	Leu54, Ala88
BCI-XI	PHPI-Cl	-8.4	1.757	2.957	Lys20, Glu44, Ala50, Ala95
Urease	AHPI-Br	-10.3	1.531	1.872	Ala16, Thr33, Val36, Ala37, Lys704, Met734, Leu827
Urease	POMPI-F	-9.7	2.16	5.079	Ala37, Lys704, Leu827

**Fig. 5** Human Bcl-x1 protein complexed with PHPI (A) and PHPI-Cl (B). Surface representation of the protein structure displays ligand bound in the active site cavity of the receptor (left) and 3D interaction of ligand and receptor showing key interactions (right).

apoptosis is the condensation of the nucleus and its fragmented segments (Taylor et al., 2008). Therefore, our results indicated that PHPI-I and PHPI-Cl could act as a promising anti-cancer agent by targeting apoptotic cell death mechanism.

The SwissADME server used for ADME analysis of imidazole derivatives was useful to highlight the drug-likeness properties. According to previous studies, compounds with molecular weight  $\leq 500$  g/mol, recommended Log S (aqueous solubility) between  $-6.5$ – $0.5$ , HBD between 0 and 6 and HBA between 2 and 10, and Lipophilicity (Log P) to predict BBB permeability as well as gastrointestinal (GI) absorption  $\leq 5$ , and TPSA  $\leq 140$  Å<sup>2</sup> are considered as optimal drug candi-

dates (Alghamdi et al., 2021; Bouchery and Harris, 2019). Comparing the SwissADME reports, it was observed that the targeted compounds to be sub-optimal for toxicity for drug-likeness properties Fig. 10.

### 3. Experimental section

#### 3.1. Chemistry

All the chemicals obtained from commercial suppliers were used as received unless noted. Reaction progress was moni-

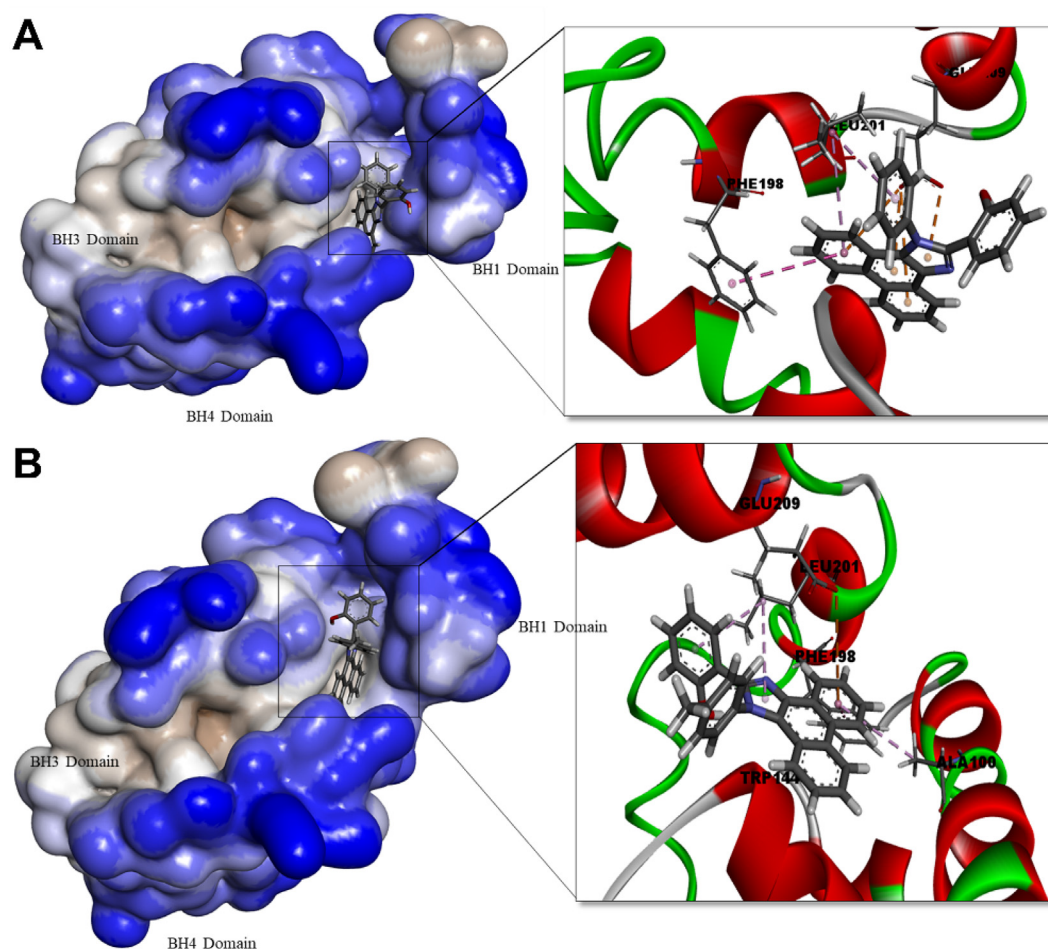


**Fig. 6** Human Bcl-2 protein complexed with PHPI (A) and PHPI-Cl (B). Surface representation of the protein structure displays ligand bound in the active site cavity of the receptor (left) and 3D interaction of ligand and receptor showing key interactions (right).

tored by using thin-layer chromatography (TLC) with commercial TLC plates (silica gel 60 F254, Merck Co.) and Chromatography was used to purify the product on silica gel (60–120 mesh). Chemical structures of the synthesized molecules were confirmed by  $^1\text{H}$  and  $^{13}\text{C}$  NMR recorded on Bruker 300 MHz, and Oxford 400 MHz NMR instruments, high-resolution GC-mass spectrometry obtained from JEOL, JMS-AX505WA, and elemental analysis measured on CE Instrument, EA2220. Melting range measurements were collected from DegiMelt MPA161 instrument.

**3.2. General procedure for the synthesis of  $\pi$ -extended phenanthro[9,10-*d*],  $\pi$ -fused acenaphtho[1,2-*d*], and  $\pi$ -non fused tetra phenyl imidazoles.**

**Scheme 1** describes the synthesis of imidazole derivatives and the compounds with varying functional groups are listed in **Table 1**.  $\alpha$ -diketone (1 eq.) and ammonium acetate (5 eq.) were added into a magnetically stirred solution of aryl aldehyde (1 eq.) and arylamine (1 eq.) in glacial acetic acid, at room temperature under nitrogen atmosphere. Refluxed the reaction mixture at 120 °C for 12 h and the progress was monitored by using TLC. After completion, the reaction mixture was cooled and poured into a copious amount of

water. Filtered the product and washed with water until neutral pH. After then the product was dissolved in dichloromethane and dried over anhydrous sodium sulfate. Removed the solvent under reduced pressure to get the crude product and purified by column chromatography on silica gel using hexane–ethyl acetate mixture as eluent. Crystallization from ethyl acetate afforded crystalline solid by slow evaporation technique.

### 3.2.1. 7-(4-fluorophenyl)-8-phenyl-7H-acenaphtho[1,2-*d*]imidazole (ATPI-F)

Orange crystalline solid. **Melting Range:** 187–190 °C.  $^1\text{H}$  NMR (300 MHz,  $\text{CDCl}_3$ ):  $\delta$  7.96 (d,  $J$  = 6.8 Hz, 1H), 7.71 (dd,  $J$  = 7.7, 4.6 Hz, 2H), 7.56 (dd,  $J$  = 8.3, 6.9 Hz, 1H), 7.52 – 7.45 (m, 4H), 7.37 (dd,  $J$  = 8.3, 7.0 Hz, 1H), 7.34 – 7.27 (m, 3H), 7.24 – 7.14 (m, 3H);  $^{13}\text{C}$  NMR (75 MHz,  $\text{CDCl}_3$ ):  $\delta$  164.08 (s), 160.77 (s), 150.67 (s), 148.09 (s), 138.63 (s), 134.16 (d,  $J$  = 3.2 Hz), 131.74 (s), 130.55 (d,  $J$  = 12.0 Hz), 129.67 (s), 129.00 – 128.41 (m), 128.24 – 127.86 (m), 127.04 (dd,  $J$  = 23.5, 12.8 Hz), 121.04 (s), 118.81 (s), 117.24 (s), 116.94 (s), 77.65 (s), 77.23 (s), 76.81 (s). **MS (EI) calcd. for  $\text{C}_{25}\text{H}_{15}\text{FN}_2$ :** 362.12; **found:** 362 [ $\text{M}^+$ ]. **Elemental analysis calcd. for  $\text{C}_{25}\text{H}_{15}\text{FN}_2$ :** C, 82.86; H, 4.17; F, 5.24; N, 7.73; **found:** C, 82.09; H, 4.34; N, 7.50.

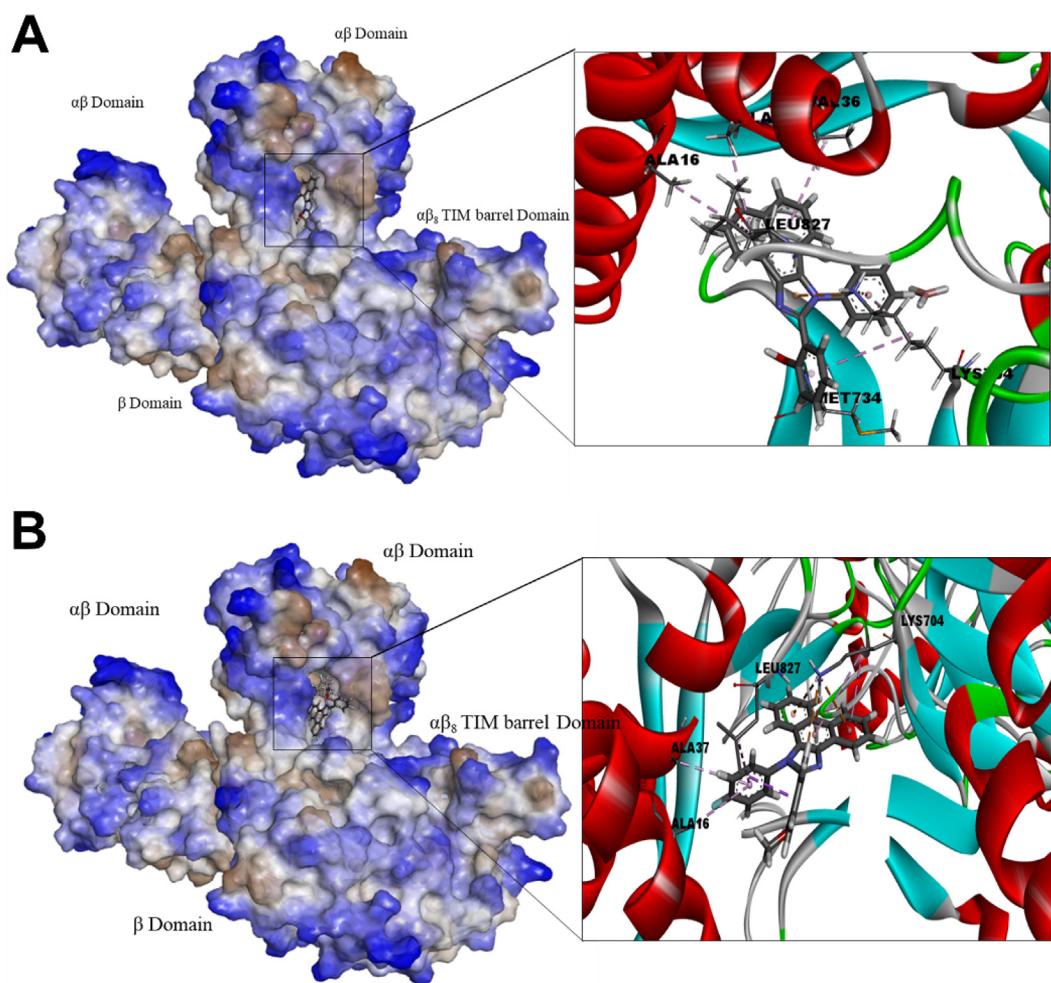


**Fig. 7** Jack bean (*Canavalia ensiformis*) urease docked with POMPI-F (A), and AHPI-Br (B). Surface representation of the protein structure displays ligand bound in the active site cavity of the receptor (left) and 3D interaction of ligand and receptor showing key interactions (right).

### 3.2.2. 7-(4-fluorophenyl)-8-(2-methoxyphenyl)-7H-acenaphtho[1,2-d]imidazole (AOMPI-F)

Orange crystalline solid. **Melting Range:** 183–185 °C. **<sup>1</sup>H NMR (300 MHz, CDCl<sub>3</sub>):** δ 7.91 (d, *J* = 6.8 Hz, 1H), 7.74–7.64 (m, 3H), 7.55 (dd, *J* = 8.3, 6.9 Hz, 1H), 7.35 (ddd, *J* = 15.7, 11.5, 6.4 Hz, 5H), 7.08 (dt, *J* = 18.1, 7.9 Hz, 3H), 6.75 (d, *J* = 8.3 Hz, 1H), 3.38 (s, 3H). **<sup>13</sup>C NMR (75 MHz, CDCl<sub>3</sub>):** δ 163.74–163.35 (m), 160.35–159.95 (m), 156.89 (s), 148.91 (s), 148.18 (s), 137.31 (s), 134.66 (s), 132.36 (s), 131.60 (s), 131.06 (d, *J* = 19.4 Hz), 129.67 (s), 128.04 (s), 127.53–126.81 (m), 126.81–126.18 (m), 120.93 (d, *J* = 18.7 Hz), 120.20 (s), 118.84 (s), 116.33 (s), 116.03 (s), 110.98 (s), 77.65 (s), 77.23 (s), 76.81 (s), 54.90 (s). **MS (EI) calcd. for C<sub>25</sub>H<sub>17</sub>FN<sub>2</sub>O:** 392.13; **found:** 392 [M<sup>+</sup>]. **Elemental analysis calcd. for C<sub>25</sub>H<sub>17</sub>FN<sub>2</sub>O:** C, 79.58; H, 4.37; F, 4.84; N, 7.14; O, 4.08; **found:** C, 79.52; H, 4.48; N, 7.11; O, 5.30.

### 3.2.3. 2-(7-phenyl-7H-acenaphtho[1,2-d]imidazol-8-yl)phenol (AHPI)

Orange crystalline solid. **Melting Range:** 200–203 °C. **<sup>1</sup>H NMR (300 MHz, CDCl<sub>3</sub>):** δ 12.88 (s, 1H), 7.91 (d, *J* = 6.8 Hz, 1H),

7.72 (t, *J* = 8.5 Hz, 2H), 7.68–7.53 (m, 6H), 7.39–7.29 (m, 1H), 7.21–6.98 (m, 3H), 6.81 (d, *J* = 9.2 Hz, 1H), 6.53 (t, *J* = 8.2 Hz, 1H). **<sup>13</sup>C NMR (75 MHz, CDCl<sub>3</sub>):** δ 158.06 (s), 148.56 (s), 145.26 (s), 137.51 (s), 133.82 (s), 131.73 (s), 130.33 (s), 129.65 (d, *J* = 8.0 Hz), 128.45 (s), 128.11 (s), 127.74 (s), 127.24 (s), 126.38 (s), 125.98 (s), 123.69 (s), 121.53 (s), 119.32 (s), 118.47 (d, *J* = 4.3 Hz), 118.16 (s), 113.58 (s), 77.65 (s), 77.23 (s), 76.81 (s). **MS (EI) calcd. for C<sub>25</sub>H<sub>16</sub>N<sub>2</sub>O:** 360.13; **found:** 361 [M<sup>+</sup>]. **Elemental analysis calcd for C<sub>25</sub>H<sub>16</sub>N<sub>2</sub>O:** C, 83.31; H, 4.47; N, 7.77; O, 4.44; **found:** C, 83.5322; H, 4.4733; N, 7.6054; O, 4.5530.

### 3.2.4. 2-(7-(4-fluorophenyl)-7H-acenaphtho[1,2-d]imidazol-8-yl)phenol (AHPI-F)

Orange crystalline solid. **Melting Range:** 208–210 °C. **<sup>1</sup>H NMR (300 MHz, CDCl<sub>3</sub>):** δ 12.79 (s, 1H), 7.85 (d, *J* = 6.9 Hz, 1H), 7.68 (dd, *J* = 8.3, 6.4 Hz, 2H), 7.59–7.47 (m, 3H), 7.38–7.24 (m, 3H), 7.22–7.04 (m, 2H), 6.98 (d, *J* = 6.9 Hz, 1H), 6.75 (dd, *J* = 8.1, 1.6 Hz, 1H), 6.60–6.48 (m, 1H). **<sup>13</sup>C NMR (75 MHz, CDCl<sub>3</sub>):** δ 158.10 (s), 148.68 (s), 144.98 (s), 138.28 (s), 134.44 (s), 131.72 (s), 130.22 (s), 129.66 (s), 128.70 (d, *J* = 8.7 Hz),

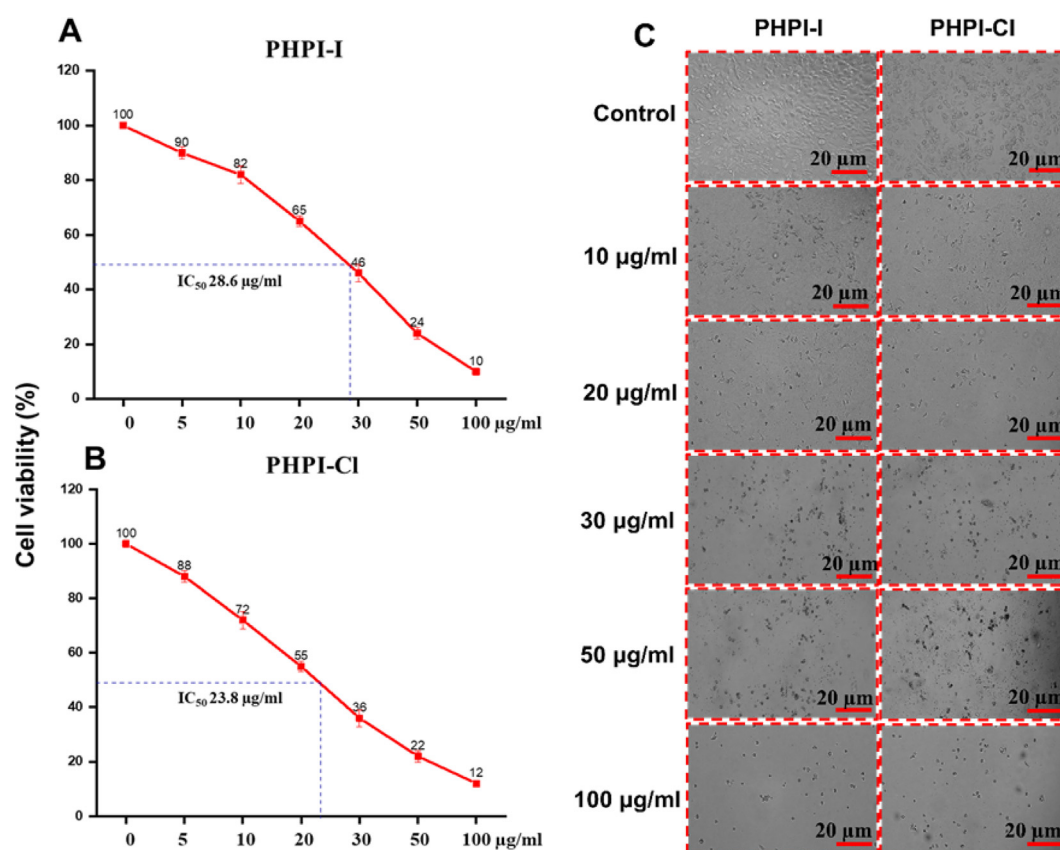


**Fig. 8** Cell viability and morphological changes with or without PHPI or PHPI-CI treatment. **A.** PHPI-I treatment, **B.** PHPI-CI treatment, and **C.** Morphological characteristics of AGS cell lines were observed in a dose dependent manner with or without PHPI-I or PHPI-CI treatment. The experiment was carried out independently in triplicates and the represented images were shown.

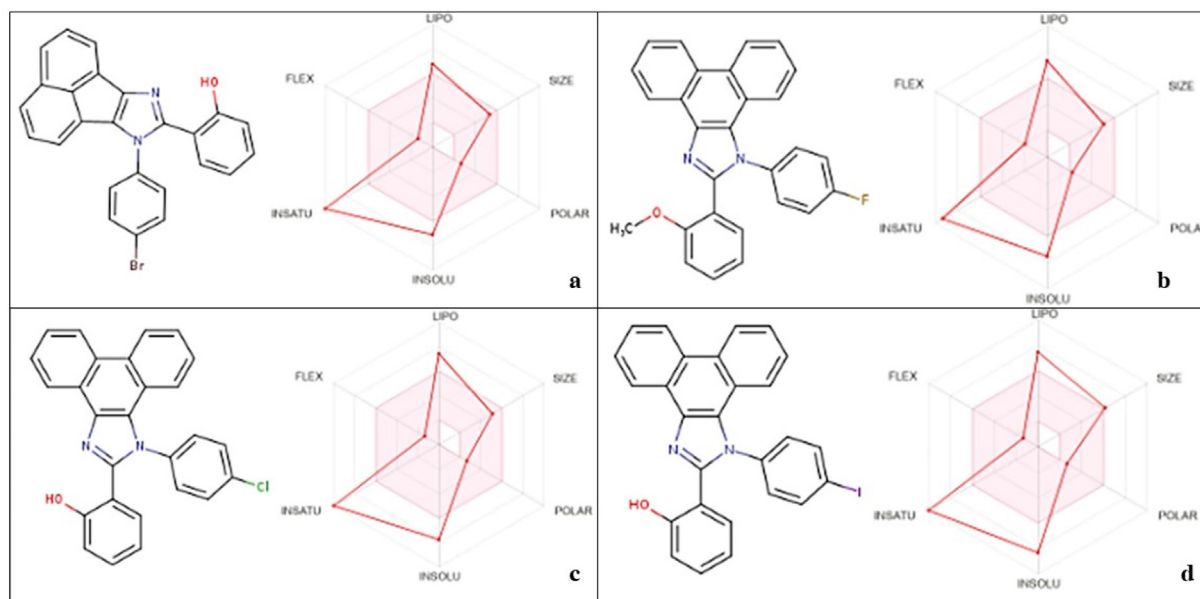


**Fig. 9** In-silico ADME analysis of potential derivatives represents the drug likeness parameters lying in the feasible region (presented in the pink region) a. AHPI-Br; b. POMPI-F; c. PHPI-CI; d. PHPI-I.

128.07 (s), 127.64 (s), 127.16 (s), 126.42 (s), 125.79 (s), 121.43 (s), 119.19 (s), 118.33 (s), 118.06 (s), 117.78 (s), 117.48 (s), 113.66 (s). **MS (EI) calcd. for C<sub>25</sub>H<sub>15</sub>FN<sub>2</sub>O:** 378.12; **found:**

379 [M<sup>+</sup>]; **Elemental analysis calcd. C<sub>25</sub>H<sub>15</sub>FN<sub>2</sub>O:** C, 79.35; H, 4.00; F, 5.02; N, 7.40; O, 4.23; **found:** C, 79.3584; H, 4.1151; N, 7.4210; O, 4.3217.

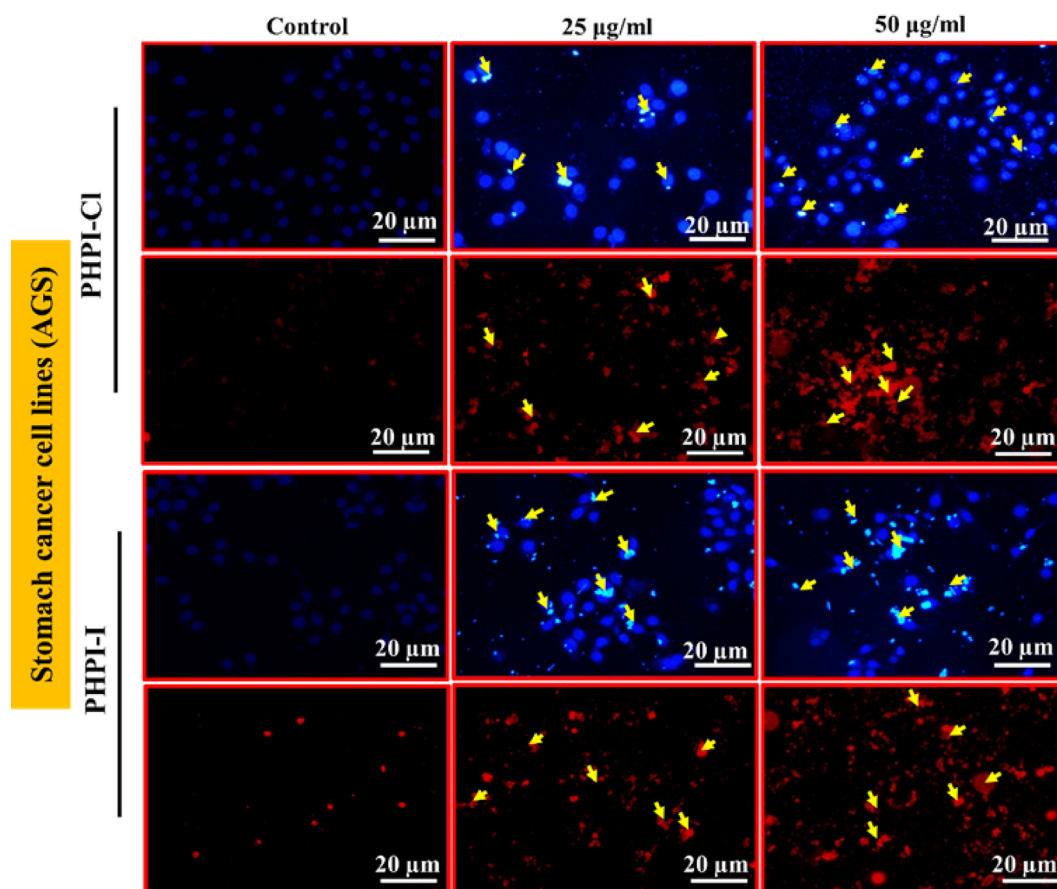


**Fig. 10** Hoechst and Propidium iodide (PI) staining of AGS cells. Arrow indicates the cell death after PHPI or PHPI-CI treatment. The experiment was carried out independently in triplicates and the represented images were shown.

3.2.5. 2-(7-(4-chlorophenyl)-7H-acenaphtho[1,2-d]imidazol-8-yl)phenol (AHPI-Cl)

Orange crystalline solid. **Melting Range:** 195–199 °C.  $^1\text{H}$  NMR (300 MHz,  $\text{CDCl}_3$ ):  $\delta$  12.70 (s, 1H), 7.88 (d,  $J$  = 6.8 Hz, 1H), 7.72 (dd,  $J$  = 8.2, 6.5 Hz, 2H), 7.66–7.47 (m, 5H), 7.35 (dd,  $J$  = 8.3, 7.0 Hz, 1H), 7.18 (ddd,  $J$  = 8.6, 7.0, 1.6 Hz, 1H), 7.13–7.00 (m, 2H), 6.79 (dd,  $J$  = 8.1, 1.6 Hz, 1H), 6.63–6.51 (m, 1H).  $^{13}\text{C}$  NMR (75 MHz,  $\text{CDCl}_3$ ):  $\delta$  158.08 (s), 148.62 (s), 136.99 (s), 135.73 (s), 130.84 (s), 130.32 (s), 129.70 (s), 128.15 (d,  $J$  = 4.6 Hz), 127.74 (s), 127.21 (s), 126.40 (s), 125.95 (s), 121.53 (s), 119.30 (s), 118.42 (s), 118.11 (s).  $\delta$  158.08 (s), 148.62 (s), 145.23 (s), 138.09 (s), 136.99 (s), 135.73 (s), 131.74 (s), 130.84 (s), 130.32 (s), 129.66 (d,  $J$  = 6.5 Hz), 128.15 (d,  $J$  = 4.6 Hz), 127.74 (s), 127.21 (s), 126.40 (s), 125.95 (s), 121.53 (s), 119.30 (s), 118.42 (s), 118.11 (s), 113.61 (s), 77.65 (s), 77.23 (s), 76.81 (s). **MS (EI) calcd. for  $\text{C}_{25}\text{H}_{15}\text{ClN}_2\text{O}$ :** 394.09; **found:** 394 [ $\text{M}^+$ ]. **Elemental analysis calcd. for  $\text{C}_{25}\text{H}_{15}\text{ClN}_2\text{O}$ :** C, 76.05; H, 3.83; Cl, 8.98; N, 7.09; O, 4.05; **found:** C, 76.1480; H, 3.9217; N, 7.0767; 4.1521.

3.2.6. 2-(7-(4-bromophenyl)-7H-acenaphtho[1,2-d]imidazol-8-yl)phenol (AHPI-Br)

Orange crystalline solid. **Melting Range:** 202–212 °C.  $^1\text{H}$  NMR (300 MHz,  $\text{CDCl}_3$ ):  $\delta$  12.68 (s, 1H), 7.88 (d,  $J$  = 6.8 Hz, 1H), 7.73 (dd,  $J$  = 17.1, 7.8 Hz, 4H), 7.61–7.52 (m, 1H), 7.45 (d,  $J$  = 8.6 Hz, 2H), 7.40–7.29 (m, 1H), 7.18 (t,  $J$  = 7.7 Hz, 1H), 7.07 (dd,  $J$  = 12.1, 7.6 Hz,

2H), 6.79 (d,  $J$  = 7.1 Hz, 1H), 6.57 (t,  $J$  = 7.1 Hz, 1H).  $^{13}\text{C}$  NMR (75 MHz,  $\text{CDCl}_3$ ):  $\delta$  158.06 (s), 148.56 (s), 145.26 (s), 137.51 (s), 133.82 (s), 131.73 (s), 130.33 (s), 129.65 (d,  $J$  = 8.0 Hz), 128.45 (s), 128.11 (s), 127.74 (s), 127.23 (d,  $J$  = 2.7 Hz), 126.38 (s), 125.98 (s), 123.69 (s), 121.53 (s), 119.32 (s), 118.44 (s), 118.11 (s), 113.58 (s), 77.65 (s), 77.23 (s), 76.81 (s). **MS (EI) calcd. for  $\text{C}_{25}\text{H}_{15}\text{BrN}_2\text{O}$ :** 438.04; **found:** 440 [ $\text{M}^+$ ]. **Elemental analysis calcd. for  $\text{C}_{25}\text{H}_{15}\text{BrN}_2\text{O}$ :** C, 68.35; H, 3.44; Br, 18.19; N, 6.38; O, 3.64; **found:** C, 68.2480; H, 3.3396; N, 6.4046; 3.2327.

3.2.7. 2-(7-(4-iodophenyl)-7H-acenaphtho[1,2-d]imidazol-8-yl)phenol (AHPI-I)

Orange crystalline solid. **Melting Range:** 225–229 °C.  $^1\text{H}$  NMR (300 MHz,  $\text{CDCl}_3$ ):  $\delta$  12.66 (s, 1H), 7.95 (d,  $J$  = 8.5 Hz, 2H), 7.87 (d,  $J$  = 6.8 Hz, 1H), 7.71 (dd,  $J$  = 8.0, 6.6 Hz, 2H), 7.55 (dd,  $J$  = 8.1, 7.0 Hz, 1H), 7.38–7.27 (m, 3H), 7.23–7.14 (m, 1H), 7.07 (dd,  $J$  = 10.3, 7.7 Hz, 2H), 6.79 (dd,  $J$  = 8.0, 1.2 Hz, 1H), 6.58 (t,  $J$  = 8.1 Hz, 1H).  $^{13}\text{C}$  NMR (75 MHz,  $\text{CDCl}_3$ ):  $\delta$  158.04 (s), 148.50 (s), 145.29 (s), 139.76 (s), 138.06 (d,  $J$  = 19.8 Hz), 131.72 (s), 130.32 (s), 129.63 (d,  $J$  = 7.5 Hz), 128.59 (s), 128.10 (s), 127.73 (s), 127.23 (s), 126.37 (s), 126.02 (s), 121.57 (s), 119.34 (s), 118.44 (s), 118.10 (s), 113.58 (s), 95.13 (s), 77.65 (s), 77.23 (s), 76.81 (s). **MS (EI) calcd. for  $\text{C}_{25}\text{H}_{15}\text{IN}_2\text{O}$ :** 488.03; **found:** 487 [ $\text{M}^+$ ]. **Elemental analysis calcd. for  $\text{C}_{25}\text{H}_{15}\text{IN}_2\text{O}$ :** C, 61.74; H, 3.11; I, 26.10; N, 5.76; O, 3.29; **found:** C, 60.8052; H, 3.3026; N, 5.8802; O, 3.1908.

3.2.8. 4-(8-(2-hydroxyphenyl)-7H-acenaphtho[1,2-d]imidazol-7-yl)phenethyl acetate (AHPI-EtOAc)

Orange crystalline solid. **Melting Range:** 147–150 °C. <sup>1</sup>H NMR (300 MHz, CDCl<sub>3</sub>): δ 12.87 (s, 1H), 7.88 (d, *J* = 6.8 Hz, 1H), 7.70 (t, *J* = 7.9 Hz, 2H), 7.61–7.41 (m, 5H), 7.39–7.28 (m, 1H), 7.21–6.97 (m, 3H), 6.80 (d, *J* = 8.8 Hz, 1H), 4.43 (t, *J* = 6.9 Hz, 2H), 3.12 (t, *J* = 6.9 Hz, 2H), 2.09 (s, 3H). <sup>13</sup>C NMR (75 MHz, CDCl<sub>3</sub>): δ 170.93 (s), 157.90 (s), 148.47 (s), 144.74 (s), 139.68 (s), 138.16 (s), 136.71 (s), 131.62 (s), 130.79 (s), 129.90 (s), 129.54 (d, *J* = 10.1 Hz), 127.86 (s), 127.36 (s), 127.27–126.31 (m), 125.77 (s), 121.15 (s), 119.11 (s), 118.05 (s), 117.77 (s), 113.68 (s), 77.45 (s), 77.03 (s), 76.61 (s), 64.36 (s), 34.89 (s), 20.93 (s). **MS (EI) calcd. for C<sub>29</sub>H<sub>24</sub>N<sub>2</sub>O<sub>3</sub>:** 446.16; **found:** 447 [M<sup>+</sup>]. **Elemental analysis calcd. for C<sub>29</sub>H<sub>24</sub>N<sub>2</sub>O<sub>3</sub>:** C, 78.01; H, 4.97; N, 6.27; O, 10.75; **found:** C, 78.4048; H, 4.8514; N, 7.0181; O, 8.0108.

3.2.9. 4-methoxy-2-(7-phenyl-7H-acenaphtho[1,2-d]imidazol-8-yl)phenol (AMHPI)

Orange crystalline solid. **Melting Range:** 162–165 °C. <sup>1</sup>H NMR (300 MHz, CDCl<sub>3</sub>): δ 12.39 (s, 1H), 7.87 (d, *J* = 6.8 Hz, 1H), 7.61 (dq, *J* = 15.2, 8.2 Hz, 8H), 7.36–7.27 (m, 1H), 7.04–6.95 (m, 2H), 6.75 (dd, *J* = 8.9, 3.0 Hz, 1H), 6.32 (d, *J* = 2.9 Hz, 1H), 3.27 (s, 3H). <sup>13</sup>C NMR (75 MHz, CDCl<sub>3</sub>): δ 152.21 (s), 151.39 (s), 148.52 (s), 145.05 (s), 138.42 (d, *J* = 17.3 Hz), 131.84 (s), 130.59 (s), 129.72 (d, *J* = 10.8 Hz), 128.04 (s), 127.54 (s), 127.12 (d, *J* = 8.3 Hz), 126.56 (s), 121.35 (s), 119.28 (s), 118.63 (s), 117.65 (s), 113.33 (s), 109.65 (s), 77.65 (s), 77.23 (s), 76.80 (s), 55.23 (s). **MS (EI) calcd. for C<sub>26</sub>H<sub>18</sub>N<sub>2</sub>O<sub>2</sub>:** 390.14; **found:** 390 [M<sup>+</sup>]. **Elemental analysis calcd. for C<sub>26</sub>H<sub>18</sub>N<sub>2</sub>O<sub>2</sub>:** C, 79.98; H, 4.65; N, 7.17; O, 8.20; **found:** C, 79.89; H, 4.5840; N, 7.0847; O, 8.1018.

3.2.10. 1-(4-fluorophenyl)-2,4,5-triphenyl-1H-imidazole (BTPI-F)

White crystalline solid. **Melting Range:** 225–227 °C. <sup>1</sup>H NMR (300 MHz, CDCl<sub>3</sub>): δ 7.60 (d, *J* = 6.4 Hz, 2H), 7.42 (s, 2H), F 7.31–7.18 (m, 9H), 7.16–7.10 (m, 2H), 7.01 (d, *J* = 4.9 Hz, 2H), 6.98–6.91 (m, 2H). <sup>13</sup>C NMR (75 MHz, CDCl<sub>3</sub>): δ 163.85 (s), 160.47 (s), 147.22 (s), 138.55 (s), 134.48 (s), 133.34 (s), 131.31 (s), 131.03 (s), 130.44 (dd, *J* = 25.5, 9.8 Hz), 129.16 (s), 128.81–128.07 (m), 127.55 (s), 126.89 (s), 116.48 (s), 116.18 (s), 77.65 (s), 77.23 (s), 76.81 (s). **MS (EI) calcd. for C<sub>27</sub>H<sub>19</sub>FN<sub>2</sub>:** 390.15; **found:** 390 [M<sup>+</sup>]. **Elemental analysis calcd. for C<sub>27</sub>H<sub>19</sub>FN<sub>2</sub>:** C, 83.05; H, 4.90; F, 4.87; N, 7.17; **found:** C, 83.48; H, 5.08; N, 7.19.

3.2.11. 1-(4-fluorophenyl)-2-(2-methoxyphenyl)-4,5-diphenyl-1H-imidazole (BOMPI-F)

White crystalline solid. **Melting Range:** 210–214 °C. <sup>1</sup>H NMR (300 MHz, CDCl<sub>3</sub>): δ 7.60 (dd, *J* = 15.9, 8.5 Hz, 4H), 7.33 (t, *J* = 8.6 Hz, 1H), 7.26 (s, 1H), 7.26–7.16 (m, 9H), 7.14 (d, *J* = 8.0 Hz, 4H), 7.01 (t, *J* = 7.8 Hz, 2H), 6.85 (dt, *J* = 17.0, 8.2 Hz, 7H), 6.69 (d, *J* = 8.3 Hz, 2H), 3.38 (s, 5H). <sup>13</sup>C NMR (75 MHz, CDCl<sub>3</sub>): δ 157.02 (s), 145.78 (s), 138.37 (s), 134.66 (s), 133.54 (s), 132.67 (s), 131.49–130.78 (m), 129.81 (s), 129.23 (d, *J* = 8.4 Hz), 128.67 (s), 128.20 (d, *J* = 10.6 Hz), 127.70 (s), 126.69 (s), 120.92 (s), 120.33 (s), 115.41 (s), 115.11 (s), 110.71 (s), 77.65 (s), 77.23 (s), 76.81 (s), 54.85 (s). **MS (EI) calcd. for C<sub>28</sub>H<sub>21</sub>FN<sub>2</sub>O:** 420.16; **found:**

**for:** 420. [M<sup>+</sup>]. **Elemental analysis calcd. for C<sub>28</sub>H<sub>21</sub>FN<sub>2</sub>O:** C, 79.98; H, 5.03; F, 4.52; N, 6.66; O, 3.81; **found:** C, 80.43; H, 5.28; N, 6.63; O, 4.83. **Melting Range:** 210–214 °C.

3.2.12. 2-(1,4,5-triphenyl-1H-imidazol-2-yl)phenol (BHPI)

White crystalline solid. **Melting Range:** 249–255 °C. <sup>1</sup>H NMR (300 MHz, CDCl<sub>3</sub>): δ 13.47 (s, 1H), 7.58–7.51 (m, 2H), 7.42–7.35 (m, 3H), 7.28 (s, 2H), 7.25–7.22 (m, 3H), 7.22–7.17 (m, 3H), 7.16–7.11 (m, 3H), 7.10–7.04 (m, 1H), 6.57–6.50 (m, 1H), 6.50–6.42 (m, 1H). <sup>13</sup>C NMR (75 MHz, CDCl<sub>3</sub>): δ 158.64 (s), 145.12 (s), 137.34 (s), 135.37 (s), 133.30 (s), 131.53 (s), 130.65 (s), 130.37–129.55 (m), 129.39 (s), 129.12–128.24 (m), 127.16 (d, *J* = 7.5 Hz), 126.22 (s), 117.98 (d, *J* = 15.7 Hz), 113.19 (s), 77.65 (s), 77.23 (s), 76.81 (s). **MS (EI) calcd. for C<sub>27</sub>H<sub>20</sub>N<sub>2</sub>O:** 388.16; **found:** 388 [M<sup>+</sup>]. **Elemental analysis calcd. for C<sub>27</sub>H<sub>20</sub>N<sub>2</sub>O:** C, 83.48; H, 5.19; N, 7.21; O, 4.12; **found:** C, 84.10; H, 5.36; N, 7.23; O, 3.97.

3.2.13. 2-(1-(4-fluorophenyl)-4,5-diphenyl-1H-imidazol-2-yl)phenol (BHPI-F)

White crystalline solid. **Melting Range:** 217–220 °C. <sup>1</sup>H NMR (300 MHz, CDCl<sub>3</sub>): δ 13.38 (s, 3H), 7.52 (dd, *J* = 7.9, 1.5 Hz, 7H), 7.22 (dd, *J* = 14.0, 7.2 Hz, 21H), 7.18–7.07 (m, 20H), 7.07–6.98 (m, 8H), 6.57–6.43 (m, 7H). <sup>13</sup>C NMR (75 MHz, CDCl<sub>3</sub>): δ 164.30 (s), 160.99 (s), 158.65 (s), 145.20 (s), 135.47 (s), 133.24 (d, *J* = 18.1 Hz), 131.51 (s), 130.60 (d, *J* = 8.9 Hz), 130.26 (s), 129.84 (s), 128.80 (s), 128.49 (s), 127.16 (d, *J* = 18.1 Hz), 126.03 (s), 118.07 (d, *J* = 13.9 Hz), 117.03 (s), 116.72 (s), 113.00 (s), 77.65 (s), 77.23 (s), 76.81 (s). **MS (EI) calcd. for C<sub>27</sub>H<sub>19</sub>FN<sub>2</sub>O:** 406.15; **found:** 407 [M<sup>+</sup>]. **Elemental analysis calcd. for C<sub>27</sub>H<sub>19</sub>FN<sub>2</sub>O:** C, 79.79; H, 4.71; F, 4.67; N, 6.89; O, 3.94; **found:** C, 79.7581; H, 4.7778; N, 6.9205; O, 3.8991.

3.2.14. 2-(1-(4-chlorophenyl)-4,5-diphenyl-1H-imidazol-2-yl)phenol (BHPI-Cl)

White crystalline solid. **Melting Range:** 201–203 °C. <sup>1</sup>H NMR (300 MHz, CDCl<sub>3</sub>): δ 13.28 (s, 4H), 7.56–7.48 (m, 9H), 7.34 (s, 4H), 7.31 (s, 6H), 7.28 (s, 8H), 7.25 (s, 8H), 7.22 (t, *J* = 5.1 Hz, 11H), 7.17–7.03 (m, 26H), 6.59–6.46 (m, 9H). <sup>13</sup>C NMR (75 MHz, CDCl<sub>3</sub>): δ 158.61 (s), 145.12 (s), 135.79 (d, *J* = 15.8 Hz), 135.34 (s), 133.08 (s), 130.25 (dd, *J* = 25.0, 7.9 Hz), 129.76 (s), 128.87 (s), 128.51 (s), 127.21 (d, *J* = 18.3 Hz), 126.15 (s), 118.13 (d, *J* = 17.1 Hz), 112.94 (s), 77.65 (s), 77.23 (s), 76.80 (s). **MS (EI) calcd. for C<sub>27</sub>H<sub>19</sub>ClN<sub>2</sub>O:** 422.12; **found:** 423 [M<sup>+</sup>]. **Elemental analysis calcd. for C<sub>27</sub>H<sub>19</sub>ClN<sub>2</sub>O:** C, 76.68; H, 4.53; Cl, 8.38; N, 6.62; O, 3.78; **found:** C, 76.5001; H, 4.6113; N, 6.7546; O, 3.6899.

3.2.15. 2-(1-(4-bromophenyl)-4,5-diphenyl-1H-imidazol-2-yl)phenol (BHPI-Br)

White crystalline solid. **Melting Range:** 217–222 °C. <sup>1</sup>H NMR (300 MHz, CDCl<sub>3</sub>): δ 13.25 (s, 3H), 7.50 (dd, *J* = 11.0, 8.0 Hz, 14H), 7.35–7.18 (m, 22H), 7.17–7.07 (m, 12H), 7.03 (d, *J* = 8.5 Hz, 8H), 6.52 (q, *J* = 8.1 Hz, 7H). <sup>13</sup>C NMR (75 MHz, CDCl<sub>3</sub>): δ 158.60 (s), 145.07 (s), 136.41 (s), 135.73 (s), 133.06 (s), 131.51 (s), 130.39 (t, *J* = 3.7 Hz), 129.73 (s), 128.89 (s), 128.51 (s), 127.22 (d, *J* = 18.3 Hz), 126.18 (s), 123.41 (s), 118.14 (d, *J* = 18.3 Hz), 112.92 (s), 77.65 (s), 77.23 (s), 76.81 (s). **MS (EI) calcd. for C<sub>27</sub>H<sub>19</sub>BrN<sub>2</sub>O:** 466.07;

**found:** 467 [M<sup>+</sup>]. **Elemental analysis calcd. for C<sub>27</sub>H<sub>19</sub>BrN<sub>2</sub>O:** C, 69.39; H, 4.10; Br, 17.10; N, 5.99; O, 3.42; **found:** C, 69.3942; H, 4.2815; N, 6.0235; O, 3.3812.

3.2.16. 2-(1-(4-iodophenyl)-4,5-diphenyl-1H-imidazol-2-yl)phenol (BHPI-I)

White crystalline solid. **Melting Range:** 207–210 °C. **<sup>1</sup>H NMR (300 MHz, CDCl<sub>3</sub>):** δ 13.24 (s, 1H), 7.68 (d, *J* = 8.4 Hz, 2H), 7.51 (d, *J* = 6.5 Hz, 2H), 7.26 (dq, *J* = 13.8, 6.8 Hz, 7H), 7.12 (ddd, *J* = 12.9, 9.9, 7.5 Hz, 4H), 6.91 (d, *J* = 8.4 Hz, 2H), 6.59 – 6.48 (m, 2H). **<sup>13</sup>C NMR (75 MHz, CDCl<sub>3</sub>):** δ 158.59 (s), 145.05 (s), 139.04 (s), 137.12 (s), 135.77 (s), 133.09 (s), 131.52 (s), 130.78 – 130.21 (m), 129.75 (s), 128.91 (s), 128.51 (s), 127.24 (d, *J* = 16.7 Hz), 126.23 (s), 118.16 (d, *J* = 19.3 Hz), 112.94 (s), 94.98 (s), 77.65 (s), 77.23 (s), 76.81 (s). **MS (EI) calcd. for C<sub>27</sub>H<sub>19</sub>IN<sub>2</sub>O:** 514.05; **found:** 515 [M<sup>+</sup>]. **Elemental analysis calcd. for C<sub>27</sub>H<sub>19</sub>IN<sub>2</sub>O:** C, 63.05; H, 3.72; I, 24.67; N, 5.45; O, 3.11; **found:** C, 69.3942; H, 4.2815; N, 6.0235; O, 3.6832.

3.2.17. 1-(4-fluorophenyl)-2-phenyl-1H-phenanthro[9,10-d]imidazole (PTPI-F)

White crystalline solid. **Melting Range:** 231–233 °C. **<sup>1</sup>H NMR (300 MHz, CDCl<sub>3</sub>):** δ 8.87 (d, *J* = 8.0 Hz, 2H), 8.78 (d, *J* = 7.9 Hz, 2H), 8.71 (d, *J* = 8.4 Hz, 2H), 7.78 – 7.71 (m, 2H), 7.70 – 7.62 (m, 2H), 7.60 – 7.45 (m, 10H), 7.36 – 7.27 (m, 10H), 7.26 (s, 1H), 7.20 (d, *J* = 8.3 Hz, 2H). **<sup>13</sup>C NMR (75 MHz, CDCl<sub>3</sub>):** δ 164.77 (s), 161.45 (s), 151.30 (s), 137.60 (s), 134.89 (d, *J* = 3.6 Hz), 131.07 (d, *J* = 8.7 Hz), 130.51 (s), 129.56 (d, *J* = 13.1 Hz), 129.16 (s), 128.63 – 128.09 (m), 127.43 (d, *J* = 14.7 Hz), 126.52 (s), 125.89 (s), 125.17 (s), 124.39 (s), 123.44 – 122.79 (m), 120.79 (s), 117.53 (s), 117.22 (s), 77.65 (s), 77.23 (s), 76.81 (s). **MS (EI) calcd. for C<sub>27</sub>H<sub>17</sub>FN<sub>2</sub>:** 388.14; **found:** 388 [M<sup>+</sup>]. **Elemental analysis calcd. for C<sub>27</sub>H<sub>17</sub>FN<sub>2</sub>:** C, 83.49; H, 4.41; F, 4.89; N, 7.21; **found:** C, 83.74; H, 4.60; N, 7.19.

3.2.18. 1-(4-fluorophenyl)-2-(2-methoxyphenyl)-1H-phenanthro[9,10-d]imidazole (POMPI-F)

White crystalline solid. **Melting Range:** 210–214 °C. **<sup>1</sup>H NMR (300 MHz, CDCl<sub>3</sub>):** δ 8.85 (d, *J* = 8.0 Hz, 1H), 8.78 (d, *J* = 8.4 Hz, 1H), 8.71 (d, *J* = 8.3 Hz, 1H), 7.72 (t, *J* = 7.5 Hz, 1H), 7.68 – 7.59 (m, 1H), 7.52 (dd, *J* = 8.1, 6.6 Hz, 2H), 7.45 – 7.26 (m, 5H), 7.12 (t, *J* = 8.5 Hz, 2H), 6.99 (t, *J* = 7.5 Hz, 1H), 6.76 (d, *J* = 8.4 Hz, 1H), 3.57 (s, 3H). **<sup>13</sup>C NMR (75 MHz, CDCl<sub>3</sub>):** δ 157.63 (s), 150.23 (s), 137.65 (s), 134.42 (s), 132.65 (s), 131.53 (s), 130.51 (d, *J* = 8.7 Hz), 129.35 (s), 128.31 (s), 127.51 (d, *J* = 8.4 Hz), 126.42 (s), 125.67 (s), 125.08 (s), 124.35 (s), 123.40 – 122.88 (m), 120.80 (d, *J* = 18.5 Hz), 120.13 (s), 116.36 (s), 116.06 (s), 110.68 (s), 77.65 (s), 77.23 (s), 76.81 (s), 55.10 (s). **MS (EI) calcd. for C<sub>28</sub>H<sub>19</sub>FN<sub>2</sub>O:** 418.15; **found:** 418 [M<sup>+</sup>]. **Elemental analysis calcd. for C<sub>28</sub>H<sub>19</sub>FN<sub>2</sub>O:** C, 80.37; H, 4.58; F, 4.54; N, 6.69; O, 3.82; **found:** C, 80.76; H, 4.82; N, 6.68; O, 4.87.

3.2.19. 2-(1-phenyl-1H-phenanthro[9,10-d]imidazol-2-yl)phenol (PHPI)

White crystalline solid. **Melting Range:** 192–194 °C. **<sup>1</sup>H NMR (300 MHz, CDCl<sub>3</sub>):** δ 13.87 (s, 3H), 8.76 (d, *J* = 8.3 Hz, 4H), 8.73 – 8.65 (m, 8H), 7.81 – 7.71 (m, 15H), 7.71 – 7.66 (m, 5H),

7.63 (ddd, *J* = 6.5, 3.9, 1.5 Hz, 9H), 7.51 (ddd, *J* = 8.4, 7.0, 1.3 Hz, 4H), 7.27 (d, *J* = 1.2 Hz, 1H), 7.25 – 7.17 (m, 7H), 7.13 (dd, *J* = 8.3, 1.3 Hz, 4H), 7.04 (dd, *J* = 8.4, 0.8 Hz, 4H), 6.73 (dd, *J* = 8.2, 1.5 Hz, 4H), 6.54 – 6.46 (m, 4H). **<sup>13</sup>C NMR (75 MHz, CDCl<sub>3</sub>):** δ 159.40 (s), 148.60 (s), 139.24 (s), 134.58 (s), 131.19 – 130.55 (m), 129.64 (s), 129.25 (s), 128.61 (s), 127.67 (s), 127.21 (s), 126.70 (s), 126.24 (s), 125.96 (s), 125.43 (s), 124.35 (s), 123.38 (s), 122.75 (s), 121.04 (s), 118.23 (s), 113.29 (s), 77.65 (s), 77.23 (s), 76.81 (s). **MS (EI) calcd. for C<sub>27</sub>H<sub>18</sub>N<sub>2</sub>O:** 386.14; **found:** 386 [M<sup>+</sup>]. **Elemental analysis calcd. for C<sub>27</sub>H<sub>18</sub>N<sub>2</sub>O:** C, 83.92; H, 4.69; N, 7.25; O, 4.14; **found:** C, 83.24; H, 5.30; N, 6.81; O, 4.89.

3.2.20. 2-(1-(4-fluorophenyl)-1H-phenanthro[9,10-d]imidazol-2-yl)phenol (PHPI-F)

White crystalline solid. **Melting Range:** 187–189 °C. **<sup>1</sup>H NMR (300 MHz, CDCl<sub>3</sub>):** δ 13.73 (s, 1H), 8.75 (d, *J* = 8.4 Hz, 1H), 8.68 (d, *J* = 8.9 Hz, 2H), 7.75 (t, *J* = 7.6 Hz, 1H), 7.68 (d, *J* = 7.2 Hz, 1H), 7.66 – 7.48 (m, 3H), 7.41 (t, *J* = 8.4 Hz, 2H), 7.30 (d, *J* = 7.4 Hz, 1H), 7.26 (d, *J* = 4.4 Hz, 1H), 7.21 (d, *J* = 7.0 Hz, 1H), 7.13 (d, *J* = 8.1 Hz, 1H), 7.05 (d, *J* = 8.3 Hz, 1H), 6.71 (d, *J* = 8.1 Hz, 1H), 6.54 (t, *J* = 7.6 Hz, 1H). **<sup>13</sup>C NMR (75 MHz, CDCl<sub>3</sub>):** δ 165.32 (s), 161.98 (s), 159.38 (s), 148.69 (s), 135.21 (d, *J* = 3.5 Hz), 134.64 (s), 131.45 – 130.92 (m), 129.68 (s), 128.60 (s), 127.73 (s), 127.14 (s), 126.79 (s), 126.58 – 125.73 (m), 125.54 (s), 124.46 (s), 123.37 (s), 122.68 (d, *J* = 8.6 Hz), 120.78 (s), 118.35 (s), 118.05 (s), 113.11 (s), 77.65 (s), 77.23 (s), 76.81 (s). **MS (EI) calcd. for C<sub>27</sub>H<sub>17</sub>FN<sub>2</sub>O:** 404.13; **found:** 404 [M<sup>+</sup>]. **Elemental analysis calcd. for C<sub>27</sub>H<sub>17</sub>FN<sub>2</sub>O:** C, 80.18; H, 4.24; F, 4.70; N, 6.93; O, 3.96; **found:** C, 80.39; H, 4.40; N, 6.87; O, 4.96.

3.2.21. 2-(1-(4-chlorophenyl)-1H-phenanthro[9,10-d]imidazol-2-yl)phenol (PHPI-Cl)

White crystalline solid. **Melting Range:** 200–204 °C. **<sup>1</sup>H NMR (300 MHz, CDCl<sub>3</sub>):** δ 13.68 (s, 1H), 8.76 (d, *J* = 8.3 Hz, 1H), 8.69 (d, *J* = 8.2 Hz, 2H), 7.81 – 7.63 (m, 4H), 7.61 – 7.47 (m, 3H), 7.31 (t, *J* = 7.3 Hz, 1H), 7.24 – 7.18 (m, 1H), 7.10 (dd, *J* = 18.0, 8.1 Hz, 2H), 6.73 (dd, *J* = 8.1, 1.3 Hz, 1H), 6.62 – 6.50 (m, 1H). **<sup>13</sup>C NMR (75 MHz, CDCl<sub>3</sub>):** δ 159.33 (s), 148.55 (s), 137.73 (s), 136.83 (s), 134.73 (s), 131.20 (d, *J* = 18.5 Hz), 130.64 (s), 129.66 (s), 128.59 (s), 127.72 (s), 126.93 (d, *J* = 14.8 Hz), 126.23 (d, *J* = 17.5 Hz), 125.70 (d, *J* = 19.5 Hz), 124.46 (s), 123.36 (s), 122.64 (d, *J* = 14.9 Hz), 120.78 (s), 118.37 (d, *J* = 3.5 Hz), 113.03 (s), 77.65 (s), 77.23 (s), 76.81 (s). **MS (EI) calcd. for C<sub>27</sub>H<sub>17</sub>ClN<sub>2</sub>O:** 420.10; **found:** 420 [M<sup>+</sup>]. **Elemental analysis calcd. for C<sub>27</sub>H<sub>17</sub>ClN<sub>2</sub>O:** C, 77.05; H, 4.07; Cl, 8.42; N, 6.66; O, 3.80; **found:** C, 77.05; H, 4.10; N, 6.58; O, 4.05.

3.2.22. 2-(1-(4-bromophenyl)-1H-phenanthro[9,10-d]imidazol-2-yl)phenol (PHPI-Br)

White crystalline solid. **Melting Range:** 211–212 °C. **<sup>1</sup>H NMR (300 MHz, CDCl<sub>3</sub>):** δ 13.63 (s, 1H), 8.72 (dd, *J* = 22.5, 8.4 Hz, 3H), 7.85 (d, *J* = 8.4 Hz, 2H), 7.71 (dt, *J* = 15.3, 7.1 Hz, 2H), 7.52 (dd, *J* = 16.5, 7.9 Hz, 3H), 7.31 (t, *J* = 7.7 Hz, 1H), 7.22 (d, *J* = 8.2 Hz, 1H), 7.10 (dd, *J* = 16.7, 8.3 Hz, 2H), 6.72 (d, *J* = 8.1 Hz, 1H), 6.56 (t, *J* = 7.6 Hz, 1H). **<sup>13</sup>C NMR (75 MHz, CDCl<sub>3</sub>):** δ 159.37 (s), 148.59 (s), 138.33 (s), 134.85 (s), 134.38



(s), 131.05 (d,  $J = 12.1$  Hz), 129.75 (s), 128.67 (s), 127.79 (s), 126.98 (d,  $J = 11.8$  Hz), 126.62 – 125.78 (m), 125.63 (s), 124.94 (s), 124.52 (s), 123.41 (s), 122.71 (d,  $J = 15.3$  Hz), 120.86 (s), 118.40 (s), 113.08 (s), 77.65 (s), 77.23 (s), 76.80 (s). **MS (EI) calcd. for  $C_{27}H_{17}BrN_2O$ :** 464.05; **found:** 465 [ $M^+$ ]. **Elemental analysis calcd for  $C_{27}H_{17}BrN_2O$ :** C, 69.69; H, 3.68; Br, 17.17; N, 6.02; O, 3.44; **found:** C, 69.9066; H, 3.6637; N, 6.3926; O, 3.5286.

### 3.2.23. 2-(1-(4-iodophenyl)-1H-phenanthro[9,10-d]imidazol-2-yl)phenol (PHPI-I)

White crystalline solid. **Melting Range:** 223–226 °C.  **$^1H$  NMR (300 MHz,  $CDCl_3$ ):**  $\delta$  13.63 (s, 1H), 8.70 (dd,  $J = 22.3, 8.4$  Hz, 3H), 8.04 (d,  $J = 8.3$  Hz, 2H), 7.70 (dt,  $J = 25.3, 7.5$  Hz, 2H), 7.52 (t,  $J = 7.7$  Hz, 1H), 7.31 (dd,  $J = 12.9, 8.2$  Hz, 3H), 7.21 (d,  $J = 8.2$  Hz, 1H), 7.10 (dd,  $J = 16.6, 8.2$  Hz, 2H), 6.71 (d,  $J = 8.0$  Hz, 1H), 6.56 (t,  $J = 7.6$  Hz, 1H).  **$^{13}C$  NMR (75 MHz,  $CDCl_3$ ):**  $\delta$  159.35 (s), 148.53 (s), 140.34 (s), 139.00 (s), 134.84 (s), 131.11 (s), 129.71 (s), 127.77 (s), 126.95 (d,  $J = 8.7$  Hz), 126.29 (d,  $J = 15.2$  Hz), 125.88 (s), 125.61 (s), 124.49 (s), 123.40 (s), 122.69 (d,  $J = 15.4$  Hz), 120.86 (s), 118.41 (d,  $J = 4.7$  Hz), 113.07 (s), 96.47 (s), 77.65 (s), 77.23 (s), 76.81 (s). **MS (EI) calcd. for  $C_{27}H_{17}IN_2O$ :** 512.04; **found:** 513 [ $M^+$ ]. **Elemental analysis calcd for  $C_{27}H_{17}IN_2O$ :** C, 63.30; H, 3.34; I, 24.77; N, 5.47; O, 3.12; **found:** C, 62.0275; H, 3.3624; N, 5.5396; O, 3.2086.

### 3.3. Photophysical properties

Absorption and photoluminescence emission spectra were obtained from Scinco (S-4100 model) UV–vis spectrometer and Scinco (FS2 model) fluorescence spectrophotometer respectively. The fluorescence spectra were corrected for the instrumental response. The quantum yields were calculated by measuring the integrated area under the emission curve and by using following equation (1): Where ' $\Phi$ ' is the quantum yield, ' $I$ ', the integrated emission intensity, ' $OD$ ', the optical density at the excitation wavelength, and ' $\eta$ ' is the refractive index of the solvent. The subscript 'standard' and 'sample' refer to the fluorophore of reference and unknown, respectively. In this case, the unknown is all the imidazole molecules displayed in scheme and the reference is quinine sulfate ( $\Phi_f = 0.54$  in 0.1 M  $H_2SO_4$ ). Optically matched solutions with very similar optical densities of the "sample" and "standard" at a given absorbing wavelength were used for quantum yield calculations.

### 3.4. Computational studies

In the present work, the theoretical investigation of the all the electronic structure calculations and geometrical properties was performed with the Gaussian 09 package (Frisch et al., 2009). The geometry optimization of the  $\pi$ -expanded phenanthro[9,10-d],  $\pi$ -fused acenaphtho[1,2-d], and  $\pi$ -non fused tetra-substituted imidazoles were performed using the DFT method, and the electronically excited state was performed depending on Self Consistent Field-Time Dependent-DFT (SCF-TD-DFT) method using Becke's three-parameter hybrid exchange functional (Becke, 1993) and Lee, and Yang and Parr correlation functional (Lee et al., 1988) B3LYP/6-

31G (d, p). The spin density distributions were visualized using Gaussview 5.0.8.

### 3.5. Urease inhibition assay

The Jack bean urease activity was determined by measuring the amount of ammonia produced with the indophenols method described by Weatherburn *et. al.* The reaction mixtures, comprising 20  $\mu$ L of the enzyme (Jack bean urease, 5 U/mL) and 20  $\mu$ L of compounds in 50  $\mu$ L buffer (100 mM urea, 0.01 M  $K_2HPO_4$ , 1 mM EDTA, and 0.01 M LiCl, pH 8.2), were incubated for 30 min at 37 °C in 96-well plate. Briefly, 50  $\mu$ L each of phenol reagents (1%, w/v phenol and 0.005%, w/v sodium nitroprusside) and 50  $\mu$ L of alkali reagent (0.5%, w/v NaOH and 0.1% Sodium hypochlorite NaOCl) were added to each well. The absorbance at 625 nm was measured after 10 min, using a microplate reader (OPTI Max, Tunable). All reactions were performed in triplicate. The urease inhibition activities were calculated according to the following formula (2): Where  $OD_{control}$  and  $OD_{sample}$  represent the optical densities in the absence and presence of the sample, respectively. Thiourea was used as the standard inhibitor for urease.

### 3.6. Kinetic mechanism study

Kinetic analysis was carried out to determine the mode of inhibition. The two inhibitors (AHPI-Br and POMPI-F) were selected based on the most potent  $IC_{50}$  values. Kinetics was carried out by varying the concentration of urea in the presence of different concentrations of compound AHPI-Br (0.00, 0.0145, and 0.029  $\mu$ M) compound POMPI-F (0.00, 0.0145, and 0.029  $\mu$ M). In detail, the urea concentration was changed from 100, 50, 25, 12.5, 6.25, and 3.125 mM for urease kinetics studies and the remaining procedure were kept the same for all kinetic studies as described in urease inhibition assay protocol. Maximal initial velocities were determined from the initial linear portion of absorbance up to 10 min after the addition of enzyme at per minute's interval. The inhibition type on the enzyme was assayed by the Lineweaver-Burk plot of inverse of velocities ( $1/V$ ) versus the inverse of substrate concentration  $1/[S]$   $mM^{-1}$ . The EI dissociation constant  $K_i$  was determined by a secondary plot of  $1/V$  versus inhibitor concentration and ESI dissociation constant  $K_i'$  was calculated by intercept versus inhibitors concentrations. Urease activity was determined by measuring ammonia production using the indophenol method as reported previously (Saeed et al., 2015). The results (change in absorbance per min) were processed by using SoftMaxPro.

### 3.7. Molecular docking

#### 3.7.1. Preparation of ligands receptors

The structural files of desired ligands PHPI, PHPI-Cl, AHPI-Br, and POMPI-F were retrieved from NCBI-PubChem in. sdf format and they were stored as.pdb after changing the structural file format. These ligands were imported and processed as ligands using ligand processing in the AutoDockTools-1.5.7. The final processed ligands were stored as.pdbqt for docking studies. The 3D structures of Bcl-2 (PDB

ID: 6QGH), Bcl-xl (PDB ID: 1R2D), and Urease (PDB ID: 4H9M) were retrieved from RCSB-Protein Data Bank. Each protein structure was observed, co-crystal ligands and heteroatoms were removed, missing residues and H-atoms were added, and the structure was saved as.pdb format. The structure was further optimized for energy minimization using Chimera-UCSF tool using algorithm steepest descent followed by conjugate gradient for 100 cycles each. The optimized models were checked for any sort of visual distortion in the main chain, side chains, and loops on the Discovery studio visualizer. The quality check of the optimized structure was performed on the SAVES server. Prior to docking of selected receptors, the docking program was validated by re-docking of co-crystal ligand allowing RMSD of 2 Å as cut-off criteria. The optimized receptor structures were imported to AutoDockTools-1.5.7 for generating the binding grids. The following coordinates were used for generating binding grids: (i) for Bcl- xl  $\times = 23.104$ ,  $y = 7.353$ , and  $z = 74.408$  (Azam et al., 2014; Bekker et al., 2021); for Bcl-2  $\times = -0.137$ ,  $y = -5.074$ , and  $z = 12.452$  (Katz et al., 2008; Kirubhanand et al., 2020; Liu et al., 2022; Yang et al., 2011); and for Urease  $\times = 1.511$ ,  $y = -55.461$ , and  $z = -26.593$  (Rashid et al., 2020; Sultan et al., 2020), (Rashid et al., 2020; Sultan et al., 2020) (Rashid et al., 2020; Sultan et al., 2020) (Rashid et al., 2020; Sultan et al., 2020) (Rashid et al., 2020; Sultan et al., 2020) (Rashid et al., 2020; Sultan et al., 2020). Kollman and Gasteiger(-Marsili) charges were added to respective proteins in.pdbqt format. Selection of the docking sites for each protein was selected as per literature reviews and grid box with desired configurations (in respective config.txt form) were prepared (Ahmed and Jami, 2012; Gurudutta et al., 2005; Rashid et al., 2020; Saxena et al., 2013; Sultan et al., 2020). The processed structures were stored as.pdbqt files for docking purposes.

### 3.7.2. Molecular docking studies

The molecular docking of ligands with receptor was done using Autodock vina v.1.2.0. that was run from the command line with configuration of grid point spacing = 0.375 Å. The exhaustiveness value of the docking was 8. The cut-off limits for the RMSD were considered as 2 Å. The output files obtained were analysed visually using Discovery studio visualizer 2019 Client. The 2-D and 3-D images illustrating the best interaction were snapped.

### 3.8. Anti-proliferative activity

The anti-proliferative activity of synthesized imidazole derivatives against the human stomach cancer cell (AGS) were evaluated using an MTT assay as our previous study [75,76].  $2 \times 10^4$  cells per well were plated in a 96 well plates containing 100  $\mu$ L of the complete culture medium. Next day, the test compounds of different concentration were added onto 96 well plates. The final concentration of DMSO Hybri-Max in all assays was less than 0.1%. 100  $\mu$ L MTT reagent was added to each well and then incubated for 3 h. MTT solution was removed and 200  $\mu$ L DMSO was added to each well. The DMSO solution is used as a negative control. The optical density values were recorded using a VersaMax microplate reader (Molecular Devices, Sunnyvale, CA, USA) at a 560 nm and

670 nm respectively. Blank values were subtracted from experimental values. The morphological observation of both treated and untreated AGS cell lines was observed through by Leica light microscope DM2000 (Wetzlar, Germany).

### 3.9. Apoptotic cell death detection

As per previous study by Balusamy et al., [75, 76] hoechst and propidium iodide staining analysis were performed. The cells  $5 \times 10^4$ /well of AGS cells were seeded and apoptosis induction was measured as stated. The selected compounds from significant  $IC_{50}$  value such as, PHPI-Cl and PHPI-I at different concentration (25 and 50  $\mu$ g/ml) were used to analyze apoptotic cell death detection. Control wells were treated only 0.1% DMSO. Fluorescent image of AGS cells which was involved in apoptotic cell death analysis was identified by Leica DMLB fluorescence microscope (Wetzlar, Germany).

### 3.10. ADME drug likeness studies

SwissADME online web server (<http://www.swissadme.ch>) was used for in-silico analysis of toxicity and pharmacokinetic properties of the potential compounds. The 2D chemical structure and SMILES formats of each compound were uploaded and program was run for the analysis. The one output panels on the web server provides a compilation of parametric values related to physicochemical properties, lipophilicity, pharmacokinetics, drug-likeness and medicinal chemistry for each compound was observed (Daina et al., 2017).

## 4. Conclusion

In summary, a series of tetra-substituted imidazole derivatives were designed, synthesized, studied their photo physical and biological activities. Among that PHP-I and PHPI-Cl showed excellent anticancer activity *in vitro* that was re-confirmed by molecular docking studies. PHP-I and PHPI-Cl has the ability to inhibit the growth of AGS cells by initiating apoptosis mediated cell death. Whereas, AHPI-Br and POMPI-F showed urease inhibitory activity *in vitro* and docking with the jack bean urease protein further confirms *in vitro* results. We believe that these compounds can be a potential target for cancer and capable of inhibiting urease enzyme, therefore recommended to test *in vivo*, that aids further use in clinical practice.

## Declaration of Competing Interest

The authors declare that they have no known competing financial interests or personal relationships that could have appeared to influence the work reported in this paper.

## Acknowledgements

This work was supported by the National Research Foundation of Korea (NRF) grant funded by the Korea government (MSIT) (No. 2021R1A2C1008375 and No. 2020R1F1A1050024).

## Appendix A. Supplementary material

Supplementary data to this article can be found online at <https://doi.org/10.1016/j.arabjc.2023.105030>.

## References

- Ahmed, M., Jami, K., 2012. BCL-2 as target for molecular docking of some neoplastic drugs. *Open Access Sci. Reports* 1, 458.
- Alarcos, N., Gutierrez, M., Liras, M., Sánchez, F., Douhal, A., 2015. An abnormally slow proton transfer reaction in a simple HBO derivative due to ultrafast intramolecular-charge transfer events. *Phys. Chem. Chem. Phys.* 17, 16257–16269. <https://doi.org/10.1039/C5CP00577A>.
- Alghamdi, S.S., Suliman, R.S., Almutairi, K., Kahtani, K., Aljatli, D., 2021. Imidazole as a promising medicinal scaffold: current status and future direction. *Drug Des. Devel. Ther.* 15, 3289–3312. <https://doi.org/10.2147/DDDT.S307113>.
- Ali, I., Lone, M.N., Aboul-Enein, H.Y., 2017. Imidazoles as potential anticancer agents. *Medchemcomm* 8, 1742–1773.
- Azam, S.S., Abro, A., Tanvir, F., Parvaiz, N., 2014. Identification of unique binding site and molecular docking studies for structurally diverse Bcl-xL inhibitors. *Med. Chem. Res.* 23, 3765–3783. <https://doi.org/10.1007/s00044-014-0957-5>.
- Becke, A.D., 1993. Density-functional thermochemistry. III. The role of exact exchange. *J. Chem. Phys.* 98, 5648–5652. <https://doi.org/10.1063/1.464913>.
- Bekker, G.-J., Fukuda, I., Higo, J., Fukunishi, Y., Kamiya, N., 2021. Cryptic-site binding mechanism of medium-sized Bcl-xL inhibiting compounds elucidated by McMD-based dynamic docking simulations. *Sci. Rep.* 11, 5046. <https://doi.org/10.1038/s41598-021-84488-z>.
- Blevins, L.K., Crawford, R.B., Bach, A., Rizzo, M.D., Zhou, J., Henriquez, J.E., Khan, D.M.I.O., Sermet, S., Arnold, L.L., Pennington, K.L., Souza, N.P., Cohen, S.M., Kaminski, N.E., 2019. Evaluation of immunologic and intestinal effects in rats administered an E 171-containing diet, a food grade titanium dioxide (TiO<sub>2</sub>). *Food Chem. Toxicol.* 133, <https://doi.org/10.1016/j.fct.2019.110793> 110793.
- Bouchery, T., Harris, N., 2019. Neutrophil–macrophage cooperation and its impact on tissue repair. *Immunol. Cell Biol.* 97, 289–298. <https://doi.org/10.1111/imcb.12241>.
- Chaudhry, D.F., Naureen, D.S., ASLAM, M., Al-Rashida, D.M., Rahman, J., Huma, D.R., Fartima, J., Khan, M., Munawar, M.A.A., Khan, D.M., 2020. Identification of imidazolopyrazole ligands as potent urease inhibitors: Synthesis, Antiurease, and in silico docking studies. *ChemistrySelect*. 5 (38), 11817–11821.
- Chen, C.-L., Cheng, Y.-F., Yu, C.-Y., Ou, H.-Y., Tsang, L.-L.-C., Huang, T.-L., Chen, T.-Y., Concejero, A., Wang, C.-C., Wang, S.-H., Lin, T.-S., Liu, Y.-W., Yang, C.-H., Yong, C.-C., Chiu, K.-W., Jawan, B., Eng, H.-L., Chan, S.C., Sharr, W.W., Lo, C.-M., Tamura, S., Sugawara, Y., Kokudo, N., Lee, K.-W., Yi, N.-J., Suh, K.-S., Moon, D.-B., Lee, S.-G., Ahn, C.-S., Huang, S., Kim, K.-H., Ha, T.-Y., Song, G.-W., Jung, D.-H., Park, G.-C., Namkoong, J.-M., Park, H.-W., Park, Y.-H., Park, C.-S., Sung, K.-B., Ko, G.-Y., Gwon, D.-I., Kaido, T., Ogawa, K., Fujimoto, Y., Ito, T., Taniyama, K., Mori, A., Ogura, Y., Uemoto, S., Yap, A.Q., Lin, Y.-H., Liu, C.-Y., Chiang, Y.-C., Lin, C.-C., Shin, M., Joh, J.-W., Kabling, C., Hu, T.-H., Kang, S.-H., Jung, B.-H., Choi, Y.-R., 2014. Living donor liver transplantation: The Asian perspective. *Transplantation* 97.
- Chowdhury, P., Panja, S., Chakravorti, S., 2003. Excited state prototropic activities in 2-hydroxy 1-naphthaldehyde. *J. Phys. Chem. A* 107, 83–90.
- Daina, A., Michielin, O., Zoete, V., 2017. SwissADME: a free web tool to evaluate pharmacokinetics, drug-likeness and medicinal chemistry friendliness of small molecules. *Sci. Rep.* 7, 42717. <https://doi.org/10.1038/srep42717>.
- Dao, P., Smith, N., Tomkiewicz-Raulet, C., Yen-Pon, E., Camacho-Artacho, M., Lietha, D., Herbeuval, J.-P., Coumoul, X., Garbay, C., Chen, H., 2015. Design, synthesis, and evaluation of novel Imidazo[1,2-a][1,3,5]triazines and their derivatives as focal adhesion kinase inhibitors with antitumor activity. *J. Med. Chem.* 58, 237–251. <https://doi.org/10.1021/jm500784e>.
- Daraji, D.G., Prajapati, N.P., Patel, H.D., 2019. Synthesis and applications of 2-substituted Imidazole and its derivatives: A review. *J. Heterocycl. Chem.* 56, 2299–2317. <https://doi.org/10.1002/jhet.3641>.
- de Laszlo, S.E., Hacker, C., Li, B., Kim, D., MacCoss, M., Mantlo, N., Pivnichny, J.V., Colwell, L., Koch, G.E., Cascieri, M.A., 1999. Potent, orally absorbed glucagon receptor antagonists. *Bioorg. Med. Chem. Lett.* 9, 641–646.
- Dipake, S.S., Ingale, V.D., Korde, S.A., Lande, M.K., Rajbhoy, A.S., Gaikwad, S.T., 2022. An efficient green protocol for the synthesis of 1,2,4,5-tetrasubstituted imidazoles in the presence of ZSM-11 zeolite as a reusable catalyst. *RSC Adv.* 12, 4358–4369. <https://doi.org/10.1039/D1RA07984K>.
- Elsässer, T., Becker, H.J., 2013. Ultrafast hydrogen bonding dynamics and proton transfer processes in the condensed phase. *Springer Science & Business Media*.
- Fernald, K., Kurokawa, M., 2013. Evading apoptosis in cancer. *Trends Cell Biol.* 23, 620–633.
- Freedman, J.E., Loscalzo, J., 2016. *New therapeutic agents in thrombosis and thrombolysis*. CRC Press.
- Frisch, M.J., Trucks, G.W., Schlegel, H.B., Scuseria, G.E., Robb, M.A., Cheeseman, J.R., Scalmani, G., Barone, V., Mennucci, B., Petersson, G.A., 2009. Gaussian 09; Gaussian, Inc. Wallingford, CT 32, 5648–5652.
- Gurudutta, G.U., Verma, Y.K., Singh, V.K., Gupta, P., Raj, H.G., Sharma, R.K., Chandra, R., 2005. Structural conservation of residues in BH1 and BH2 domains of Bcl-2 family proteins. *FEBS Lett.* 579, 3503–3507. <https://doi.org/10.1016/j.febslet.2005.05.015>.
- Hariharan, A., Kumar, S., Alagar, M., Dinakaran, K., Subramanian, K., 2018. Synthesis, photophysical and electrochemical properties of polyimides of tetraaryl imidazole. *Polym. Bull.* 75, 93–107. <https://doi.org/10.1007/s00289-017-2015-1>.
- Heeres, J., Backx, L.J.J., Mostmans, J.H., Van Cutsem, J., 1979. Antimycotic imidazoles. Part 4. Synthesis and antifungal activity of ketoconazole, a new potent orally active broad-spectrum antifungal agent. *J. Med. Chem.* 22, 1003–1005.
- Hristova, S., Dobrikov, G., Kamounah, F.S., Kawauchi, S., Hansen, P.E., Deneva, V., Nedeltcheva, D., Antonov, L., 2015. 10-Hydroxybenzo[h]quinoline: switching between single- and double-well proton transfer through structural modifications. *RSC Adv.* 5, 102495–102507. <https://doi.org/10.1039/C5RA20057A>.
- Hsieh, C.-C., Jiang, C.-M., Chou, P.-T., 2010. Recent experimental advances on excited-state intramolecular proton coupled electron transfer reaction. *Acc. Chem. Res.* 43, 1364–1374.
- Huang, C., Li, Y., Ren, H., Wang, J., Shao, L., Zhang, S., Li, G., Yang, L., 2012. Insight into the structural determinants of imidazole scaffold-based derivatives as p38 MAP kinase inhibitors by computational explorations. *Curr. Med. Chem.* 19, 4024–4037. <https://doi.org/10.2174/092986712802002608>.
- Huang, J.-D., Yu, K., Ma, H., Chai, S., Dong, B., 2017. Theoretical investigation of excited-state single and double proton transfer mechanisms for 2,5-bis(benzoxazol-2-yl)thiophene-3,4-diol. *Dye. Pigment.* 141, 441–447. <https://doi.org/10.1016/j.dyepig.2017.02.047>.
- Katz, C., Benyamini, H., Rotem, S., Lebediker, M., Danieli, T., Iosub, A., Refaely, H., Dines, M., Bronner, V., Bravman, T., Shalev, D.E., Rüdiger, S., Friedler, A., 2008. Molecular basis of the interaction between the antiapoptotic Bcl-2 family proteins and the proapoptotic protein ASPP2. *Proc. Natl. Acad. Sci.* 105, 12277–12282. <https://doi.org/10.1073/pnas.0711269105>.
- Kim, S.H., Park, S., Kwon, J.E., Park, S.Y., 2011. Organic light-emitting diodes with a white-emitting molecule: emission mechanism and device characteristics. *Adv. Funct. Mater.* 21, 644–651.
- Kim, S., Seo, J., Jung, H.K., Kim, J., Park, S.Y., 2005. White Luminescence from polymer thin films containing excited-state intramolecular proton-transfer dyes. *Adv. Mater.* 17, 2077–2082.

- Kirubhanand, C., Selvaraj, J., Rekha, U.V., Vishnupriya, V., Sivabalan, V., Manikannan, M., Nalini, D., Vijayalakshmi, P., Rajalakshmi, M., Ponnulakshmi, R., 2020. Molecular docking analysis of Bcl-2 with phyto-compounds. *Bioinformation* 16, 468–473. <https://doi.org/10.6026/97320630016468>.
- Kuila, D., Kvakovszky, G., Murphy, M.A., Vicari, R., Rood, M.H., Fritch, K.A., Fritch, J.R., Wellinghoff, S.T., Timmons, S.F., 1999. Tris (hydroxyphenyl) ethane Benzotriazole: A Copolymerizable UV light stabilizer. *Chem. Mater.* 11, 109–116.
- Lee, T.C., Yang, W.T., Parr, R.G., 1988. Density-functional crystal orbital study on the structures and energetics of polyacetylene isomers. *Phys. rev. B* 37, 785–789.
- Lin, C.-C., Chen, C.-L., Chung, M.-W., Chen, Y.-J., Chou, P.-T., 2010. Effects of multibranching on 3-hydroxyflavone-based chromophores and the excited-state intramolecular proton transfer dynamics. *J. Phys. Chem. A* 114, 10412–10420.
- Liu, X., Jiang, L., Li, Y., Huang, Y., Hu, X., Zhu, W., Wang, X., Wu, Y., Meng, X., Qi, X., 2022. Wogonin protects glomerular podocytes by targeting Bcl-2-mediated autophagy and apoptosis in diabetic kidney disease. *Acta Pharmacol. Sin.* 43, 96–110. <https://doi.org/10.1038/s41401-021-00721-5>.
- Liu, H., Wang, Y., Lv, M., Luo, Y., Liu, B., Huang, Y., Wang, M., Wang, J., 2020. Flavonoid analogues as urease inhibitors: Synthesis, biological evaluation, molecular docking studies and in-silico ADME evaluation. *Bioinorg. Chem.* 105, 104370.
- Luca, L.D., 2006. Naturally occurring and synthetic imidazoles: Their chemistry and their biological activities. *Curr. Med. Chem.* 13, 1–23.
- Machado, T.F., Serra, M.E.S., Murtinho, D., Valente, A.J.M., Naushad, M., 2021. Covalent organic frameworks: synthesis, properties and applications—An overview. *Polymers (Basel)* 13. <https://doi.org/10.3390/polym13060970>.
- Magnus, N.A., Diseroad, W.D., Nevill, C.R., Wepsiec, J.P., 2006. Synthesis of Imidazole based p38 MAP (Mitogen-Activated Protein) kinase inhibitors under buffered conditions. *Org. Process Res. & Dev.* 10, 556–560. <https://doi.org/10.1021/op060042t>.
- Mahanta, S., Singh, R.B., Kar, S., Guchhait, N., 2006. Excited state intramolecular proton transfer in 3-hydroxy-2-naphthaldehyde: a combined study by absorption and emission spectroscopy and quantum chemical calculation. *Chem. Phys.* 324, 742–752.
- Mikhailov, A.A., Kuleshov, A.V., Solyev, P.N., Korlyukov, A.A., Dorovatovskii, P.V., Mineev, K.S., Baranov, M.S., 2020. Imidazol-5-one as an acceptor in donor-acceptor cyclopropanes: Cycloaddition with aldehydes. *Org. Lett.* 22, 2740–2745. <https://doi.org/10.1021/acs.orglett.0c00725>.
- Mirjalili, B.F., Bamoniri, A.H., Zamani, L., 2012. One-pot synthesis of 1, 2, 4, 5-tetrasubstituted imidazoles promoted by nano-TiCl<sub>4</sub>. *SIOT. Sci. Iran.* 19, 565–568. <https://doi.org/10.1016/j.scient.2011.12.013>.
- Murata, T., Morita, Y., Yakiyama, Y., Fukui, K., Yamochi, H., Saito, G., Nakasuji, K., 2007. Hydrogen-bond interaction in organic conductors: redox activation, molecular recognition, structural regulation, and proton transfer in donor–acceptor charge-transfer complexes of TTF-imidazole. *J. Am. Chem. Soc.* 129, 10837–10846.
- Naureen, S., Chaudhry, F., Asif, N., Munawar, M.A., Ashraf, M., Nasim, F.H., Arshad, H., Khan, M.A., 2015. Discovery of indole-based tetraarylimidazoles as potent inhibitors of urease with low antilipoxigenase activity. *Eur. J. Med. Chem.* 102, 464–470.
- Nim, Y.S., Wong, K.-B., 2019. The maturation pathway of nickel urease. *Inorganics* 7. <https://doi.org/10.3390/inorganics7070085>.
- Pariat, T., Stoerkler, T., Diguët, C., Laurent, A.D., Jacquemin, D., Ulrich, G., Massue, J., 2021. Dual solution-/solid-state emissive excited-state intramolecular proton transfer (ESIPT) dyes: A combined experimental and theoretical approach. *J. Org. Chem.* 86, 17606–17619. <https://doi.org/10.1021/acs.joc.1c01698>.
- Park, S., Kwon, J.E., Kim, S.H., Seo, J., Chung, K., Park, S.-Y., Jang, D.-J., Medina, B.M., Gierschner, J., Park, S.Y., 2009. A white-light-emitting molecule: frustrated energy transfer between constituent emitting centers. *J. Am. Chem. Soc.* 131, 14043–14049.
- Parkin, D.M., Bray, F.I., Devesa, S.S., 2001. Cancer burden in the year 2000. The global picture. *Eur. J. Cancer* 37, 4–66.
- Peng, H.-C., Kang, C.-C., Liang, M.-R., Chen, C.-Y., Demchenko, A., Chen, C.-T., Chou, P.-T., 2011. En route to white-light generation utilizing nanocomposites composed of ultrasmall CdSe nanodots and excited-state intramolecular proton transfer dyes. *ACS Appl. Mater. Interfaces* 3, 1713–1720.
- Rashid, M., Rafique, H., Roshan, S., Shamas, S., Iqbal, Z., Ashraf, Z., Abbas, Q., Hassan, M., Qureshi, Z.U.R., Asad, M.H.H.B., 2020. Enzyme inhibitory kinetics and molecular docking studies of halo-substituted mixed ester/amide-based derivatives as jack bean urease inhibitors. *Biomed. Res. Int.* 2020. <https://doi.org/10.1155/2020/8867407>.
- Saeed, A., Zaib, S., Ashraf, S., Iftikhar, J., Muddassar, M., Zhang, K. Y.J., Iqbal, J., 2015. Synthesis, cholinesterase inhibition and molecular modelling studies of coumarin linked thiourea derivatives. *Bioorg. Chem.* 63, 58–63.
- Saxena, N., Katiyar, S.P., Liu, Y., Grover, A., Gao, R., Sundar, D., Kaul, S.C., Wadhwa, R., 2013. Molecular interactions of Bcl-2 and Bcl-xL with mortalin: identification and functional characterization. *Biosci. Rep.* 33. <https://doi.org/10.1042/BSR20130034>.
- Scarpin, M.S., Kawakami, C.M., Rangel, K.C., Pereira, K.d.C., Benevenuto, C.G., Gaspar, L.R., 2021. Effects of UV-filter photostabilizers in the photostability and phototoxicity of vitamin A palmitate combined with avobenzone and octyl methoxycinnamate. *Photochem. Photobiol.* 97, 700–709. <https://doi.org/10.1111/php.13407>.
- Schmierer, R., Mildenerger, H., Buerstell, H., 1988. German Patent 361464, 1987, in: *Chem. Abstr.* p. 37838.
- Serdaliyeva, D., Nurgozhin, T., Satbayeva, E., Khayitova, M., Seitaliyeva, A., A.L., 2022. Review of pharmacological effects of imidazole derivatives. *J. Clin. Med. Kazakhstan* 19, 11–5.
- Sharma, A., Kumar, V., Kharb, R., Kumar, S., Sharma, P.C., Pathak, D.P., 2016. Imidazole derivatives as potential therapeutic agents. *Curr. Pharm. Des.* 22, 3265–3301. <https://doi.org/10.2174/1381612822666160226144333>.
- Sharma, P., LaRosa, C., Antwi, J., Govindarajan, R., Werbovetz, K. A., 2021. Imidazoles as potential anticancer agents: An update on recent studies. *Molecules* 26, 4213.
- Sherin, P.S., Tsentalovich, Y.P., Snytnikova, O.A., Sagdeev, R.Z., 2008. Photoactivity of kynurenine-derived UV filters. *J. Photochem. Photobiol. B Biol.* 93, 127–132.
- Sherin, P.S., Grilj, J., Tsentalovich, Y.P., Vauthey, E., 2009. Ultrafast excited-state dynamics of kynurenine, a UV filter of the human eye. *J. Phys. Chem. B* 113, 4953–4962.
- Singh, R.B., Mahanta, S., Kar, S., Guchhait, N., 2007. Photo-physical properties of 1-hydroxy-2-naphthaldehyde: A combined fluorescence spectroscopy and quantum chemical calculations. *Chem. Phys.* 331, 373–384.
- Skonieczny, K., Ciuciu, A.I., Nichols, E.M., Hugues, V., Blanchard-Desce, M., Flamigni, L., Gryko, D.T., 2012. Bright, emission tunable fluorescent dyes based on imidazole and  $\pi$ -expanded imidazole. *J. Mater. Chem.* 22, 20649–20664.
- Somasundaram, S., Kamaraj, E., Hwang, S.J., Jung, S., Choi, M.G., Park, S., 2017. Synthesis, structural, and photophysical studies of  $\pi$ -fused acenaphtho[1,2-d]imidazole-based excited-state intramolecular proton transfer molecules. *J. Mol. Struct.* <https://doi.org/10.1016/j.molstruc.2017.02.025>.
- Sultan, A., Shajahan, S., Ahamad, T., Alshehri, S.M., Sajjad, N., Mehr-un-Nisa, Rehman, M.H.U., Torun, L., Khalid, M., Acevedo, R., 2020. Silica-supported heterogeneous catalysts-mediated synthesis of chalcones as potent urease inhibitors: in vitro and molecular docking studies. *Monatshefte für Chemie - Chem. Mon.* 2020 1511 151, 123–133. <https://doi.org/10.1007/S00706-019-02534-Z>.

- Sun, W., Li, S., Hu, R., Qian, Y., Wang, S., Yang, G., 2009. Understanding solvent effects on luminescent properties of a triple fluorescent ESIPT compound and application for white light emission. *J. Phys. Chem. A* 113, 5888–5895.
- Takle, A.K., Brown, M.J.B., Davies, S., Dean, D.K., Francis, G., Gaiba, A., Hird, A.W., King, F.D., Lovell, P.J., Naylor, A., Reith, A.D., Steadman, J.G., Wilson, D.M., 2006. The identification of potent and selective imidazole-based inhibitors of B-Raf kinase. *Bioorg. Med. Chem. Lett.* 16, 378–381. <https://doi.org/10.1016/j.bmcl.2005.09.072>.
- Taylor, R.C., Cullen, S.P., Martin, S.J., 2008. Apoptosis: controlled demolition at the cellular level. *Nat. Rev. Mol. Cell Biol.* 9, 231–241.
- Tolomeu, H.V., Fraga, C.A.M., 2023. Imidazole: synthesis, functionalization and physicochemical properties of a privileged structure in medicinal chemistry. *Molecules* 28. <https://doi.org/10.3390/molecules28020838>.
- Tsentalovich, Y.P., Snytnikova, O.A., Forbes, M.D.E., Chernyak, E. I., Morozov, S.V., 2006. Photochemical and thermal reactivity of kynurenine. *Exp. Eye Res.* 83, 1439–1445.
- Uenuma, S., Maeda, R., Yokoyama, H., Ito, K., 2021. Molecular recognition of fluorescent probe molecules with a pseudopolyrotaxane nanosheet. *ACS Macro Lett.* 10, 237–242. <https://doi.org/10.1021/acsmacrolett.0c00660>.
- Wang, L., Woods, K.W., Li, Q., Barr, K.J., McCroskey, R.W., Hannick, S.M., Gherke, L., Credo, R.B., Hui, Y.-H., Marsh, K., Warner, R., Lee, J.Y., Zielinski-Mozng, N., Frost, D., Rosenberg, S.H., Sham, H.L., 2002. Potent, orally active heterocycle-based combretastatin A-4 analogues: Synthesis, structure–activity relationship, pharmacokinetics, and in vivo antitumor activity evaluation. *J. Med. Chem.* 45, 1697–1711. <https://doi.org/10.1021/jm010523x>.
- Wang, Q.-D., Yang, J.-M., Zhou, B., Fang, D., Ren, J., Zeng, B.-B., 2017. Highly regioselective debus-radziszewski reaction of C-3 indole-substituted 1,2-diketones: Facile synthesis of 3-(1,2,4-Triaryl-1H-imidazol-5-yl)-indoles. *ChemistrySelect* 2, 4807–4810. <https://doi.org/10.1002/slct.201700612>.
- Wu, K.-C., Cheng, Y.-M., Lin, Y.-S., Yeh, Y.-S., Pu, S.-C., Hu, Y.-H., Yu, J.-K., Che, P.-T., 2004. Competitive intramolecular hydrogen bonding formation and excited-state proton transfer reaction in 1-[(diethylamino)-methyl]-2-hydroxy-3-naphthaldehyde. *Chem. Phys. Lett.* 384, 203–209.
- Yang, S., Liu, F., Wang, Q.J., Rosenberg, S.A., Morgan, R.A., 2011. The shedding of CD62L (L-selectin) regulates the acquisition of lytic activity in human tumor reactive T lymphocytes. *PLoS One* 6, e22560.
- Zhao, F., Lu, W., Su, F., Xu, L., Jiang, D., Sun, X., Shi, J., Zhou, M., Lin, F., Cao, F., 2018. Synthesis and potential antineoplastic activity of dehydroabietylamine imidazole derivatives. *Medchem-comm* 9, 2091–2099. <https://doi.org/10.1039/c8md00487k>.
- Zhu, J., Bienaymé, H., 2006. Multicomponent reactions. John Wiley & Sons.